



1 Remote sensing of local-dust across the Canadian Arctic

2 Seyed Ali Sayedain¹, Norman T. O'Neill¹, Keyvan Ranjbar², Phillippe Gauvin-Bourdon³, Rachel
3 Chang³, Patrick L. Hayes⁴, James King⁵

4 ¹Centre d'Applications et de Recherches en Télédétection, Université de Sherbrooke, Sherbrooke, QC, Canada

5 ²Flight Research Laboratory, National Research Council Canada, Ottawa, ON, Canada

6 ³Department of Physics and Atmospheric Science, Dalhousie University, Halifax, NS, Canada

7 ⁴Département de chimie, Université de Montréal, Montréal, QC, Canada

8 ⁵Département de géographie, Université de Montréal, Montréal, QC, Canada

9 *Correspondence to:* S. A. Sayedain (seyed.ali.sayedain@usherbrooke.ca)

10 **Abstract.**

11 We investigated the optical and microphysical characterization of High- and sub-Arctic dust events across the Canadian
12 Arctic Archipelago (CAA). Events from local sources (local dust) were first identified and characterized using a combination
13 of ground-based lidar, two AERONET instruments, and passive (MODIS, Sentinel-2, MISR) imagery in the neighbourhood
14 of the High-Arctic Polar Environment Atmospheric Research Laboratory (PEARL) at Eureka, Nunavut (on Ellesmere Island
15 in the northernmost part of the CAA).

16 The PEARL findings informed the identification and characterization of local dust events over other parts of the CAA
17 using a suite of satellite instruments whose remote sensing (RS) capabilities were complementary to or an extension of the
18 ground- and satellite-based techniques employed at Eureka. The events included plumes emanating from Axel Heiberg Island,
19 just west of Ellesmere Island, Banks Island in the southwest corner of the CAA, Ellef Ringnes Island in the eastern part of the
20 central CAA and Prince of Wales Island / Victoria Island in the central southern CAA. Plume identification, plume source and
21 CM (coarse mode) aerosol optical depth (AOD) retrievals were investigated using a combination of low to high spatial
22 resolution (MODIS to Sentinel-2) color imagery and the MODIS dark target AOD product over water. Plume thickness, height
23 and speed for most of the events were obtained (depending on orbit availability and lack of cloud contamination) from MISR
24 (Multi-angle Imaging Spectro Radiometer) stereoscopic products.

25 These RS results support an argument for the ubiquitous presence of pan-Arctic, low altitude dust that is typically (away
26 from any strong sources such as mountainous drainage basins) at the lower levels of detectability offered by ground- and
27 satellite-based RS techniques. The ability to RS airborne, near-source, local dust events and characterize dust properties and
28 dynamics of important regions such as the CAA is critical to understanding local dust impacts such as early snow/ice melt and
29 the nucleation role of local dust in the formation of low-altitude clouds.



30 **1 Introduction**

31 Local, drainage-flow dust events are recognized as an important source of dust at high latitudes (Bullard et al., 2016) and are
32 a significant contributor to Arctic and sub-Arctic aerosols in terms of total atmospheric (columnar) dust loads and notably, to
33 near-surface concentration and attendant surface deposition (Groot Zwaaftink et al., 2016). Meinander et al. (2022) employed
34 dust-transport simulations supported by recent verification data (including the identification of sources using satellite-based
35 imagery) to confirm the predominance of high-latitude dust (HLD) sources in terms of snow and ice deposition. O'Neill et al.
36 (2025) summarized satellite-derived findings of what was likely local dust deposition (with attendant decreases in visually
37 observed surface reflectance) for a sampling of drainage basin regions in the CAA. Local dust, whose source plumes can
38 produce quite strong coarse mode¹ (CM) AODs (aerosol optical depths) eventually spread out and/or are deposited to yield
39 weak, monthly-binned CM AODs (O'Neill et al., 2025 who employ the term DOD [dust optical depths] for the CM AODs
40 known to be dominated by dust).

41 Dust from Asian deserts can be transported around the world and contributes to the dust load over the Arctic (see for example
42 Uno et al., 2009). AboEl-Fetouh et al. (2020) argued that there was a small but distinct springtime, pan-Arctic (CM) AOD²
43 contribution of what was likely Asian dust over six AERONET stations spread across the Canadian and northern European
44 Arctic. They also noted that the particle-volume size distribution (PVSD) associated with those CM AODs showed a peak
45 radius $\sim 1.3 \mu\text{m}$. This feature tends to dominate monthly-binned CM AOD averages in the spring (*ibid*) while DODs associated
46 with local sources are likely more prevalent in the summer and fall according to the monthly-binned simulations (Fig. 7) of
47 Groot Zwaaftink et al. (2016)³. Aside from its rather unique temporal signature, Asian dust tends to be concentrated in weak
48 to moderately strong DOD plumes located in the mid- to upper-troposphere with some evidence of dust deposition during the
49 period of relatively strong Asian dust events (see, for example, the Fig. 3 Barrow event of Zhao et al., 2022).

50 Local dust particles in the Arctic are known to be strong ice nucleating particles (INPs) that can significantly influence the
51 dynamics of mixed-phase clouds (ice crystals and water droplets) and their optical and radiative impacts (Xi et al., 2022, Kawai
52 et al., 2023). The dust plumes lofted into the atmosphere from the Copper River Delta in southern Alaska during late summer
53 or autumn were, for example, shown to be a major INP source (Barr et al., 2023). Those authors also pointed out that the dust
54 events can last for many days and extend hundreds of kilometers into the Gulf of Alaska. Tobo et al. (2019) noted that the high
55 ice nucleating ability of local dust in the Svalbard region of the European Arctic was likely improved by the presence of organic
56 matter.

¹ Roughly speaking, particles of super μm (radius) size

² their CM AODs corresponded to integrations of the retrieved AERONET particle-volume size distribution across retrieval radii ranging from a fixed (interpolated) value of $0.6 \mu\text{m}$ (Dubovik et al., 2002) to an upper bin edge of $17.18 \mu\text{m}$ (AboEl-Fetouh et al., 2020 explicitly define the bin centers and the bin edges in their Table S1)

³ Their source and receptor regions represent broad “cap” areas that are greater than a certain latitude



57 HLD events in the Canadian Arctic and specifically the CAA are rarely monitored and so their properties are, accordingly, not
58 well characterized: low population density and limited numbers of meteorological stations have resulted in a scarcity
59 of observations. Persistent cloudy periods and the attendant underuse of RS data have represented significant challenges to the
60 exploitation of satellite RS data (Bullard et al., 2016). Alternatively, optically thinner clouds and / or surface reflectance
61 perturbations (such as white froth from waves) could act to contaminate AOD retrievals over water.

62 Satellite imagery at different spatial and temporal resolutions in the polar regions can provide color images of dust events as
63 well as plume characterization products (including AOD, plume height and thickness, coarse indicators of particle size,
64 etc.) that help to better characterize local dust. Satellite-based, high spatial-resolution RS data can, for example, enable the
65 separation of local dust-plume patterns from suspended sediments and phytoplankton blooms in the water.

66 The identification of dust plumes over the Icelandic region using MODIS true color imagery has been reported for events
67 dating back to 2002 (Arnalds, 2010). Satellite- and airborne-RS of local dust over the Arctic (as summarized by Sayedain et
68 al., 2023; SDN) include airborne RS of dust over the riverbed, fjord, and coastal regions of Svalbard, sub-Arctic dust plumes
69 flowing over the Gulf of Alaska (where they are much more readily identified and characterized), and MODIS- and CALIOP-
70 based identification of dust plumes from Iceland. A local, high-Arctic CM dust plume, induced by the drainage basin dynamics
71 of Lake Hazen (~ 300 km northeast of Eureka on Ellesmere Island), was identified and characterized by Ranjbar et al. (2021)
72 using various types of passive and active, satellite-based RS tools adapted to the special case of dust optics and microphysics.
73 Baddock et al. (2024) provided a detailed analysis of a dust event over Pearly Land, Northern Greenland employing Sentinel-
74 2 true-color images supported by reanalyzed near-surface wind and temperature data.

75 In terms of ground-based RS, Yang et al., (2020) used Doppler lidar (backscatter and depolarization ratio channels) and
76 ceilometer profiles, along with CIMEL photometry (the instrument employed by AERONET) to characterize the optical
77 properties of Icelandic, sub-Arctic dust plumes. Bachelder et al. (2020) reported peak CM radii of $\sim 1.63 \mu\text{m}$ for their measured
78 near-source particle-mass size distributions (PMSDs) of local dust in the sub-Arctic Ä'äy Chù (Slims River) basin in the
79 Canadian Yukon. SDN characterized the optical and microphysical properties of Lhù'àn Mân⁴ dust plumes using CIMEL
80 and Doppler lidar instrumentation supported by microphysical surface measurements. Their CIMEL- and lidar-derived dust
81 AODs (which we will refer to as DODs in cases where dust is likely the predominant aerosol) were CM dominated (be weaker
82 fine mode DODs that correlated with the CM DODs were also observed).

83 Kawai et al. (2023) simulated the columnar mass concentrations of local dust in the Arctic in order to lay the groundwork for
84 their investigations into the strong role of local dust as INP. They employed CALIOP profiles and the CALIOP aerosol subtype
85 classification product to produce a local-dust Arctic DOD climatology in order to verify the quality of their dust simulations.
86 Their map of simulated columnar mass abundance of pan-Arctic dust (and its conversion to CM DODs at 550 nm as per
87 O'Neill et al., 2025) helped contextualize (roughly guide or even semi-quantitatively validate) our search for dust events in

⁴ The Kluane Lake Research Station about 8 km east of the Ä'äy Chù measurement station



88 the CAA that would be detectable using satellite-based RS. In general, we expect DODs associated with local dust to be
89 dominated by CM particles (see, for example, the overview given in O'Neill et al., 2025).
90 The instruments and measurements that we employed in the investigations reported in this paper, reflect a general strategy of
91 using ground-based microphysical as well as ground-based passive and active RS measurements acquired at the High-Arctic
92 PEARL observatory as a means of demonstrating the presence of local dust in the PEARL region and then linking, by direct
93 or indirect means, this information with imagery and lidar RS products available from the very frequent overpasses of satellite-
94 based instruments over a site that is very near the tangent circle of all polar-orbiting satellites (and thus the beneficiary of a
95 high density of RS data). With this type of analysis in hand we sought to support/inform (without the ground-based RS and
96 microphysical sampling capabilities of the PEARL complex), the purely satellite-based RS and characterization of local dust
97 events in other parts of the CAA. The motivation for this work was to analyze and help verify / evaluate elements of the large
98 potential trove of satellite-based dust RS data over the CAA.

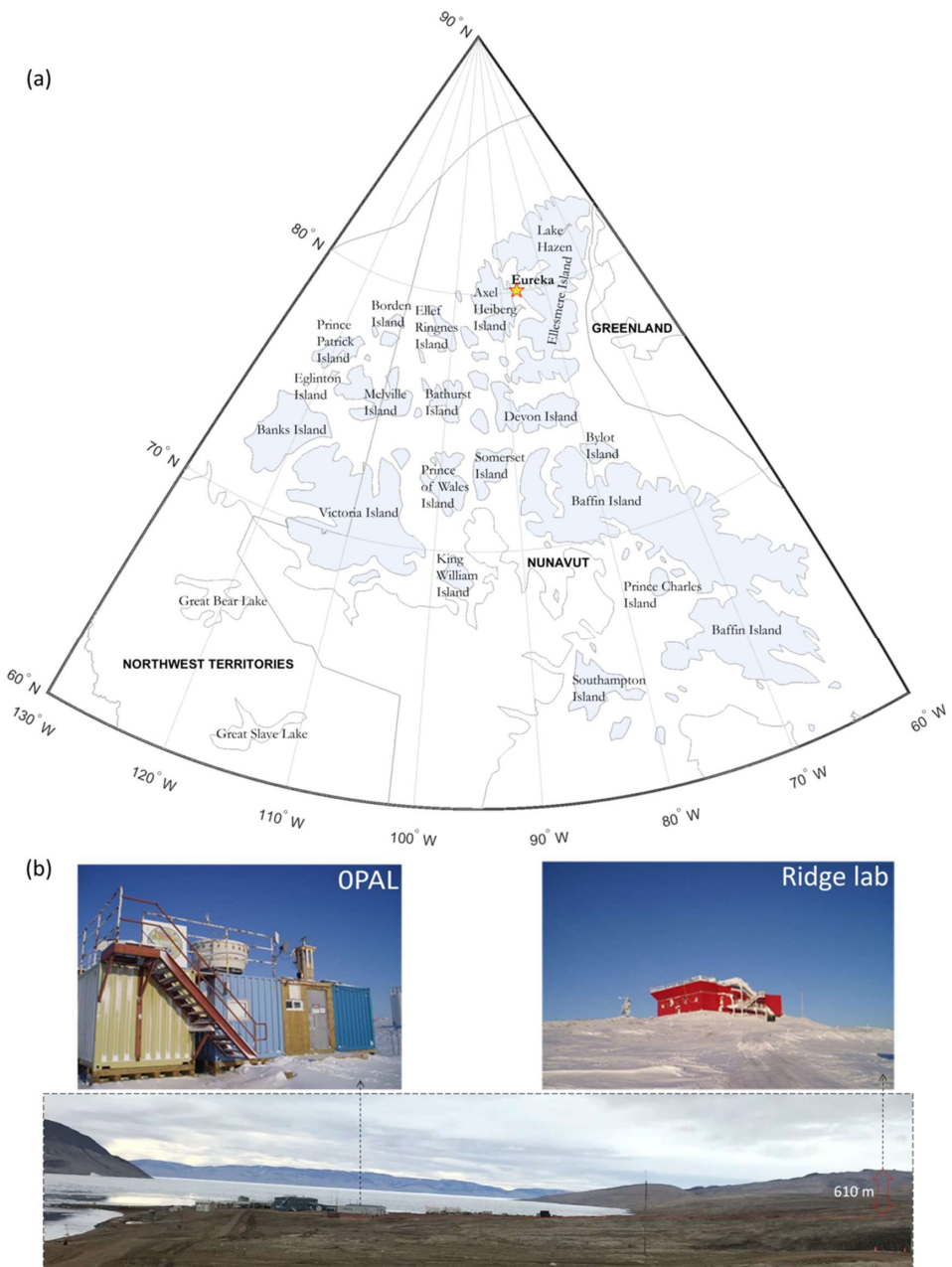
99 **2 Study Area**

100 **2.1 The Canadian Arctic Archipelago**

101 The CAA extends from the northern (low Arctic) shores of the Canadian mainland to the high Arctic near the North Pole (Fig.
102 1a). It consists of a group of approximately 36,000 islands, many of which are covered by ice for much of the year (Adams et
103 al., 2015). Different local CAA dust events at Eureka on Ellesmere Island, Axel Heiberg Island, Prince of Wales Island, Banks
104 Island, and Ellef Ringnes Island were investigated as part of this local dust analysis.

105 **2.1.1 The PEARL research complex**

106 The Polar Environment Atmospheric Research Laboratory (PEARL) at Eureka is an important High-Arctic location where
107 optical and microphysical measurements of gases, aerosols and clouds are conducted on a quasi-continuous basis. The PEARL
108 complex (indicated by a star on the map of Fig. 1a) includes two atmospheric measurement sites (Fig. 1b): the 0PAL (Zero
109 Altitude PEARL Auxiliary Laboratory) at 5 m ASL, and the Ridge lab at 615 m ASL. A 3rd measurement site known as
110 SAFIRE (Surface and Atmospheric Flux, Irradiance and Radiation Extension) is located about 5 km from 0PAL. The 0PAL
111 site and the Ridge lab are separated by a 15 km-long gravel road.





113 **Figure 1 – (a) The geographical extent of the CAA as indicated by light-blue shading. The PEARL observatory at Eureka, Nunavut**
114 **is indicated by a yellow star, (b) the PEARL complex showing both the 0PAL (left) and Ridge lab (right) sites (a wide-angle photo**
115 **of the PEARL complex is below those photos). The nominal (AERONET) coordinates of the 0PAL and Ridge lab sites are,**
116 **respectively; 79.990° N, 85.939° W at 5 m elevation and 80.054° N, 86.417° W at 615 m elevation.**

117 **3 Instrumentation & Methodology**

118 In this section, we present a brief overview of the instruments and measurements employed in our local dust investigations at
119 the PEARL complex and a summary of the satellite imagery products that we employed over targeted CAA sites in our search
120 for detectable dust events.

121 **3.1 Sun photometer / sky radiometer**

122 Spectral AOD and almucantar sky radiance measurements were acquired by two automated AERONET CIMEL sun
123 photometer/sky radiometers (see Giles et al., 2019, for recent details on the CIMEL instrument and the AERONET network).
124 The Canadian sub-network of AERONET (AEROCAN) is run by Environment and Climate Change Canada (ECCC) in
125 collaboration with AERONET. The Ridge lab and the 0PAL CIMEL have been in operation from 2007 to 2019 and from 2007
126 to the present, respectively⁵. The Ridge lab CIMEL is labeled "PEARL" in the AERONET database.

127 The CIMEL instruments acquire solar-disk irradiances across eight spectral channels from the ultraviolet (UV) to the short-
128 wave infrared (SWIR) at central wavelengths (λ) of 340, 380, 440, 500, 675, 870, 1020, and 1640 nm in a sequence of three
129 10-second (triplet) observation at a nominal temporal resolution of 3 minutes between triplets (15 min for older CIMEL
130 versions). Version 3, Level 1.0 AERONET AODs were employed in the analysis (unless otherwise stated). These AOD spectra
131 yield fine mode (FM) and coarse mode (CM) AODs (the AERONET SDA product at 500 nm wavelength) with pre-cloud-
132 screened filtering being driven by a ceiling on the variation of the triplets (see Giles et al., 2019, for AERONET processing
133 details and products).

134 The CIMELs also acquire (low frequency) AOD spectra and almucantar radiances across four spectral bands (380, 440, 675,
135 870 nm) at a nominal temporal resolution of 1 hour⁶. Version 3, Level 1.5 (cloud-screened) AOD measurements and associated
136 almucantar radiances are inverted to yield (what amount to) columnar averages of refractive index and PVSDs.

137 **3.2 Aerodynamic Particle Sizer Spectrometer**

138 The Aerodynamic Particle Sizer (APS) spectrometer measures both aerodynamic diameter and light-scattering intensity (TSI
139 Incorporated, 2022). Their basic size distribution product is a largely CM product (52 optical channels with an aerodynamic

⁵ The AERONET database name for "0PAL" is written as "OPAL"

⁶ supplemented by 4 additional AOD / almucantar measurement series at solar airmasses of 4, 3, 2 and 1.7 (Sinyuk et al., 2020).



140 particle diameter range between 0.5 to 20 μm). The chosen temporal bin-sampling frequency was 1 minute. Particle-number
141 size distributions ($dN/d\log D$) are calculated by dividing the measured number concentration of each bin by its logarithmic
142 bin size ($d\log D$). PVSD concentrations ($dv/d\log D$) are then expressed in terms of equivalent spherical particles
143 ($\frac{4}{3}\pi (D/2)^3 dN/d\log D$). CM particle-volume concentrations (v_c) are obtained by adding the $dv = PVSDs \times d\log D$ across
144 a range of CM channels⁷ ($v_c = \sum_{i=21}^{i=52} dv$).

145 3.3 Arctic High Spectral Resolution Lidar

146 The Arctic High Spectral Resolution Lidar (AHSRL) was deployed at 0PAL between August 2005 and June 2010. The AHSRL
147 employs Doppler-type lidar technology to separate (slow-moving aerosol and fast-moving molecular), velocity-induced
148 differences in Doppler frequencies. This separation enables the retrieval of particle (aerosol and/or cloud) to molecular
149 backscatter coefficient ratios that, in turn, allow for the extraction of particle backscatter profiles by the simple expediency of
150 multiplying by the relatively well-known molecular backscattering profile (Eloranta's HSRL chapter in Weitkamp, 2005). The
151 AHSRL provides backscatter coefficient⁸ (β with units of $\text{sr}^{-1} \text{ km}^{-1}$) and volume depolarization ratio (VDR⁹) profiles of 7.5 m
152 vertical resolution up to 30 km of altitude and inter-sample resolution of 1 minute (Eloranta et al., 2004). The VDR is a well-
153 known source of information related to the optical separation of FM and CM contributions to the backscatter signal. We employ
154 that type of information below to make links with CM AODs (DODs) derived from the CIMEL instruments.

155 The β altitude profiles can be integrated to yield what we refer to as the particulate backscatter optical depth (τ_β) whose FM
156 and CM AOD components are $\tau_{\beta,f}$ and $\tau_{\beta,c}$. If the FM and CM profiles are largely dominated by homogeneous particle types
157 (like, respectively, FM sulphatic-based pollution particles and CM dust) then their corresponding optical depths are given by
158 $\tau_f^l = S_f \tau_{\beta,f}$ and $\tau_c^l = S_c \tau_{\beta,c}$ (where S_f and S_c are the lidar ratios [sr] of the FM and CM particle types).

159 3.4 Satellite imagery

160 MODIS satellite images along with their derived AOD products as well as MISR multi-view images and their AOD, plume
161 height and plume speed products were employed to investigate a variety of dust events using the contextualizing diversity of
162 information layers available from the NASA Worldview¹⁰ application. High spatial resolution Sentinel-2 color images from

⁷ from bin (i) = 21 to 52. This bin range corresponds to geometric bin center diameters of $D = 1.47$ to $13.66 \mu\text{m}$. Geometric diameters are taken as the aerodynamic diameter / 1.45 (see, for example, Huang et al., 2021).

⁸ What the lidar community refers to as backscatter cross section (but which we have adapted to better fit into the extinction coefficient vocabulary of the radiative transfer community; see, for example, Hansen and Travis, 1974)

⁹ For purposes of symbolic brevity, we also employ δ to represent VDR in any equation context.

¹⁰ <https://worldview.earthdata.nasa.gov/>



163 the Copernicus Browser¹¹ were also employed on an as-needed basis: they often yielded physical and/or spatio-temporal
164 insights into local dust behavior that was not obvious in the (comparatively) low-resolution MODIS imagery and products.

165 3.4.1 MODIS

166 MODIS multispectral imagers operate on both the descending-orbit (Terra) and ascending orbit (Aqua) satellites at an altitude
167 of 705 km¹². MODIS employs 36 spectral bands between 400 nm (UV) and 14.4 μm (thermal-IR) at three different nadir
168 spatial resolutions of 250 m (bands 1–2), 500 m (bands 3–7), and 1 km (bands 8–36). The sensor has a swath width of 2330
169 km (cross-track) by 10 km (along track at nadir) and views the entire Earth every one to two days, depending on the latitude
170 of the orbit line (Justice et al., 2002). The MODIS “true color” RGB images provided by the NASA Worldview application
171 have a spatial resolution of 250 m (R = Band 1 @ 620–670 nm, G = Band 4 @ 545–565 nm, B = Band 3 @ 459–479 nm).

172 The highest-resolution, 3 km land and ocean (550 nm) AOD products (Terra, MOD04_3K, and Aqua,
173 MYD04_3K) are computed using the Dark Target (DT) algorithms over dark land and ocean targets during daytime overpasses
174 (Levy et al. 2015a, 2015b). We employed the 3 km data while monitoring the predictions of the 10 km Deep Blue (DB) AOD
175 product over Arctic land surfaces (Levy et al. 2015c, 2015d) where the DT AOD product was typically sparse or non-existent.

176 The DT algorithm’s dependence on the presence of dense dark vegetation to achieve its dark pixel threshold over land is rarely
177 achieved over the Arctic: the DB algorithm was designed to retrieve AOD over surfaces such as deserts or arid lands that are
178 bright in the visible wavelength spectrum (Sayer et al., 2014). It is tempting to employ this product given that vegetation-
179 sparse Arctic tundra often satisfies the conditions for the generation of DB AODs. However, it is a largely untested product
180 over high-Arctic sites (Sayer, 2025) and our investigations showed the presence of frequent AOD plumes (patches) that were
181 often inordinately coincident with persistently dark reflectance patterns in the imagery. In the end we relied almost exclusively
182 on the DT retrieval over water surfaces. We employed the MODIS FMF (Fine Mode Fraction) product (Song et al., 2021) as
183 a means of separating out the CM AOD from the AOD (CM AOD = (1 – FMF) \times AOD). As indicated above, the DOD is
184 generally expected to be dominated by CM particles.

185 3.4.2 MISR

186 The Multi-angle Imaging SpectroRadiometer (MISR), aboard the Terra satellite, acquires images of the same scene at nine
187 different viewing angles. The imagery is obtained at angles ranging from aft- or backward-looking (-70°) to fore- or forward-
188 looking (+70°) in four spectral bands (blue @ 447 nm, green @ 558 nm, red @ 672 nm, and near-infrared @ 867 nm).
189 The “Global Mode” nadir spatial resolution is 275 m which degrades to 1.1 km for all off-nadir bands except the red band
190 (MISR Handbook, 2000). The revisit time is every 2 to 9 days (depending on latitude) across a 380 km swath (Garay et al.,
191 2020). The stereoscopic nature of the 9 MISR images enables the extraction of plume height and plume velocity. Both
192 parameters are critical for dust plume investigations. This was notably, demonstrated by Ranjbar et al. (2021), for the case of

¹¹ <https://dataspace.copernicus.eu/browser>

¹² Local-time equatorial crossings of 10:30 a.m. and 1:30 p.m. respectively



193 a strong local-dust plume over Lake Hazen (about 330 km northeast of PEARL) that was characterized using MISR, MODIS,
194 CALIOP and CloudSat data. More detailed information on MISR stereoscopic height and wind speed retrievals and the
195 algorithm used to generate these products (the MISR INteractive eXplorer or MINX algorithm) can be found in Nelson et al.
196 (2013), who also provide case studies of plume height and wind speed retrievals for smoke, dust, and cloud.

197 It was known, from its earliest conception, that the multi-angle feature of MISR would facilitate the extraction of aerosol
198 parameters given their spatial invariance¹³ relative to the typically high frequency spatial variance and differing spectra of
199 surface reflectance (see, for example, the definitive overview of Martonchik et al., 1998). The specific stereoscopic capabilities
200 of MISR enable, in turn, the detection of aerosol or cloud plumes and the computation of their optical depth (see, for example,
201 Kahn et al., 2007, for the case of dust, smoke and volcanic plumes at the 17.6 km atmospheric processing resolution). More
202 recent versions of the MISR processing chain included a 4.4 km resolution, near real time, V23, Level 2 AOD product (Witek
203 et al., 2021) whose AODs are reported at the standard reference wavelength of 550 nm (*ibid*). We employed both the MISR
204 plume height and AOD products in our investigations of local-dust events across the CAA.

205 **4 Results & Discussion**

206 Our results are reported in two subsections: 4.1- Ground-based RS and microphysical analysis at Eureka with links to satellite-
207 based RS imagery over that site, and 4.2- Satellite-based RS of local dust events across the CAA. Our goal is to demonstrate
208 how an experienced-based local dust narrative can be built using the ground-based optical and microphysical measurements
209 of dust plumes in the Eureka region while underscoring what can be achieved using satellite-based RS data informed, as much
210 as possible, by the ground-based and satellite-based results at Eureka.

211 **4.1 Analysis of dust events at Eureka**

212 We carried out a purely optical analysis comparing CIMEL and AHSRL data¹⁴ in order to demonstrate certain optical dynamics
213 that were consistent with the apparent presence of dust particles at low elevations between 0PAL and the Ridge lab. In a
214 different sequence of events, the 0PAL CIMEL AOD measurements and in situ APS PVSDs shared a common measurement
215 period from July 9 to September 20, 2018. These two periods were an important focus of our ground-based analysis at the
216 PEARL sites. The correlation between different independent datasets was a key aspect of a multi-pronged strategy to provide
217 evidence of Arctic dust events whose RS detectability can be generally characterized as weak to marginal (O'Neill et al., 2025).

¹³ across initial atmospheric processing pixels of 17.6 km resolution

¹⁴ over the extended period that the three data sets were available (August 2005 to June 2010)



218 **4.1.1 Passive vs active (ground-based) optical analysis at Eureka**

219 Potential dust events over the period from August 2005 to June 2010 (the duration of AHSRL measurements at 0PAL) were
220 investigated by looking for low-altitude, large-amplitude VDR events whose derived CM optical depths were correlated with
221 the 0PAL CM AOD (τ_c^0) and not correlated with the PEARL CM AOD (τ_c^P) (if the plumes were found to be largely below the
222 PEARL CIMEL elevation of 615 m). The AHSRL CM AODs (τ_c^l) were obtained by integrating β_c profiles associated with
223 VDR values greater than a particular threshold (δ_{thr}) from 5 to 615 m (0PAL to Ridge lab elevations) and employing prescribed
224 FM and CM lidar ratios. The reader is directed to Appendix A1 for a discussion of the FM / CM attributions between the 0PAL
225 and PEARL CIMELs and for temporal resampling details (the resampling of τ_c^P and τ_c^l measurements to τ_c^0 times). The
226 theoretical VDR-driven FM / CM attributions for the lidar optical depths are defined in Appendix A2.

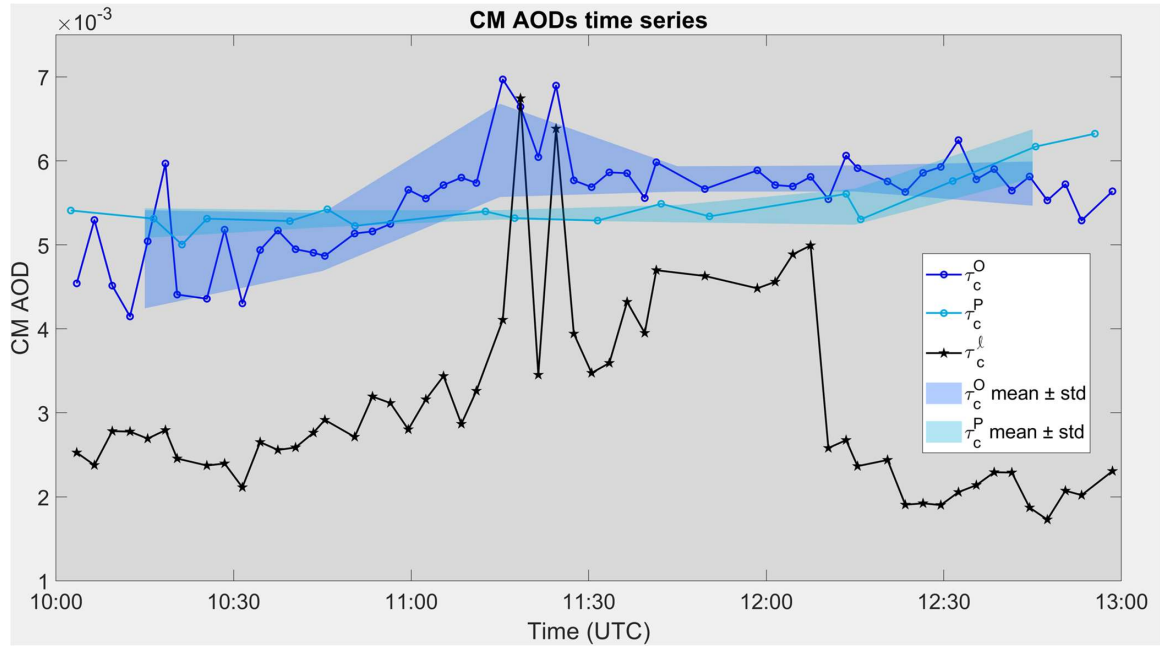
227 We analyzed the AHSRL profile statistics of 7 potential dust events in Section A3.2. The impact of varying the FM / CM
228 attribution threshold of the VDRs (the value of δ_{thr}) is detailed in Appendix A3.3¹⁵. We eventually determined that a 5% VDR
229 threshold for separating CM and FM optical depths was a reasonable compromise. The AHSRL profile details as well as the
230 corresponding derived values of τ_c^l , τ_c^0 , τ_c^P , and the 0PAL minus PEARL difference ($\Delta\tau_c$) are shown in Figures S1a to S7a¹⁶
231 while the summary (profile- and event-integrated) VDR statistics for those lidar profiles are given in Figures S1b to S7b of the
232 same file (with the overarching VDR statistics being given in the table of Fig. S8). A brief overview of those overarching
233 statistics is given in Section A3.2.

234 Figure 2 shows the calculated cloud-screened CM AOD values during the apparent dust event of July 23, 2007. We chose it
235 to illustrate the key elements in support of our dust plume detection claims. The τ_c^l and $\tau_{c,1.5}^0$ values show the high frequency
236 variations that are arguably due to near surface dust. The (high frequency) similarities between the τ_c^l and $\tau_{c,1.5}^0$ “spikes”
237 (coupled with the low frequency unresponsiveness of $\tau_{c,1.5}^P$ to those spikes) are coherent with an argument for the presence of
238 a weak, low-altitude dust event. The τ_c^l vs $\tau_{c,1.5}^0$ statistics show marginal to moderately large correlation coefficients (R values
239 from 0.41 to 0.64) for each one of the seven events (the intra-event statistics) while the inter-event correlation coefficient for
240 the ensemble of seven events was significant (R = 0.78).

241

¹⁵ Appendix A3.1 is a discussion of how we filtered (weighted) out severe outliers that could appear in the VDR profiles

¹⁶ Supplementary PowerPoint file “AHSRL_CIMEL_event_profiles”



242

243

244 **Figure 2 – Level 1.5 (cloud-screened) CM AOD time series of the July 23, 2007, dust event for the CIMELs at 0PAL ($\tau_{c,1.5}^0$) and**
 245 **PEARL ($\tau_{c,1.5}^P$) as well as the 0PAL AHSRL (τ_c^l) (altitude range of 5 to 615 m). The δ_{thr} value for separating CM and FM AODs**
 246 **was 5%. $\tau_{c,1.5}^0$ should, normally, be greater than $\tau_{c,1.5}^P$ but the nominal CIMEL accuracy of ~ 0.01 / airmass (for both the 0PAL and**
 247 **PEARL CIMELs) is a key factor in the absolute comparison of these very small CM AOD values. The solid, blue-toned bands show**
 248 **the running standard deviation about the running mean over 30-minute intervals with the first-interval mid-point starting at 10:15**
 249 **UTC¹⁷. The standard deviation of the former over the latter is significantly larger except near the end of the event (this disparity**
 250 **amounts to a quantitative check on the relative unresponsiveness of $\tau_{c,1.5}^P$)**

251 **4.1.2 Optical vs microphysical (ground-based) analysis at Eureka**

252 Figure 3 encapsulates the analysis that we carried out in the comparison of the CIMEL CM AODs and APS v_c values associated
 253 with an event that we argue was a significant dust event at Eureka. The simultaneous rise of the APS v_c values and the $\tau_{c,1.5}^0$
 254 time series after 20:30 UTC in Figures 3c and 3d are likely the start of a CM-aerosol event which this and other evidence (see
 255 Section 4.1.3) suggests was a dust event. The zoomed Fig. 3d shows a rather remarkable $\tau_{c,1.5}^0$ vs v_c correlation with departures

¹⁷ We produced these bands to focus on the high frequency differences between $\tau_{c,1.5}^0$ and $\tau_{c,1.5}^P$ (to avoid the standard deviation contributions of more low frequency variations)



256 from that correlation in the neighbourhood of $\tau_{c,1.5}^0$ and v_c peaks at, respectively, $\sim 21:30$ and $00:30$ UTC (the former could be
257 ascribed to very thin cirrus clouds that we failed to detect in any satellite data while the latter could be the result of a very
258 spatially-variable dust plume). During this particular event, two large temporal spikes were eliminated from the Level 1.0
259 retrievals by the AERONET temporally-driven (Level 1.5) cloud-screening algorithm (because the Level 1.0 AERONET
260 product of “Coarse AOD” can include CM cloud particles as well as CM aerosols¹⁸). During this particular event, two large
261 temporal spikes were eliminated from the Level 1.0 retrievals by the AERONET temporally-driven (Level 1.5) cloud-screening
262 algorithm. Supporting data for this elimination¹⁹ is presented in Figures S9 to S11 where we demonstrate that the Level 1.0
263 CM AOD spikes represent cirrus clouds that temporarily fouled the CIMEL sun-pointing FOV as determined using the MISR
264 sensor.²⁰

265 The inferred approximate position of a smaller-radius AERONET PVSD peak in Fig. 3a and the APS peak in Fig. 3b (the cyan
266 curves at 21:00 UTC) suggests a common mode peak $\sim 1.3 - 1.5 \mu\text{m}$ (with the AERONET peaks at radii $\gtrsim 6 \mu\text{m}$ being outside
267 the radius range of the APS). The $1.3 - 1.5 \mu\text{m}$ peak radius is $\sim 1.3 \mu\text{m}$ AERONET inversion peak reported by SDN in their
268 analysis of local dust at the Kluane Lake²¹ AERONET station in the Canadian Yukon (while the $6 \mu\text{m}$ AERONET peak is near
269 the upper limit of the reported KLRS peak radius range from ~ 4 to $7 \mu\text{m}$ for the 5 largest CM AOD cases; see Fig. 9 of that
270 paper). However, the KLRS CM AODs were ~ 2 to 14 times the CM AODs of the event shown in Fig. 3c (after the onset of
271 the significant rise around 20:30 UTC for which the CM AODs are ~ 0.006 to 0.016 or a $\Delta(\text{CM AOD}) \sim 0.01$). In general, dust
272 plumes in the Lhù’àn Mân’ region (associated with drainage basins of significantly greater relief than the region of Eureka)
273 demonstrated a CM AOD domination relative to the dust plumes that we claim to have found at OPAL (Fig. 3c).

274 SDN speculated that the smaller CM ($1.3 \mu\text{m}$) AERONET-inversion peak was more likely ascribable to springtime Asian dust
275 (while noting that the PVSDs measured with the TSI Optical Particle Sizer (OPS) device at KLRS showed no distinguishable
276 peak that was comparable with the $1.3 \mu\text{m}$ AERONET-inversion peak)²². However, the results presented in Fig. 3b suggest a
277 $\sim 1.4 \mu\text{m}$ (small CM) APS peak that is clearly not due to springtime Asian dust (and thus could be ascribable to
278 phenomenologically different dust PVSDs and CM AODs than those of the much more dynamic and optically strong KLRS
279 site).

¹⁸ We would point out that this is not the case for FM particles: the AERONET FM AOD product amounts to a separation of FM aerosols from CM aerosols because cloud particles do not populate this particle size range.

¹⁹ beyond the support provided in the AERONET literature for the efficacy of their cloud screening algorithm

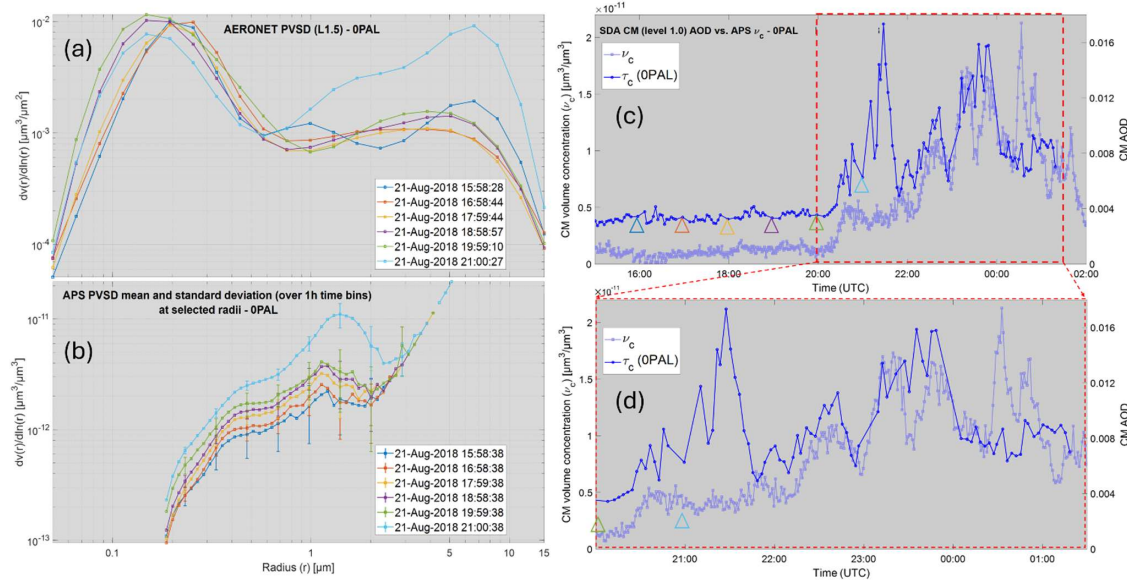
²⁰ The MISR multi-angle (stereoscopic) capabilities permitted an estimate of the time that the roughly 8 km altitude cirrus cloud (located over Axel Heiberg Island) incited a spike in the Level 1.0 CM AOD.

²¹ This is the name AERONET ascribed to the CIMEL of the Lhù’àn Mân’ region. SDN referred to the AERONET CIMEL measurements being made at KLRS (Kluane Lake Research Station): this is the place name we will associate with the “Kluane Lake” CIMEL

²² While two “Down Valley” OPCs (closer to or even a part of the source region and about 7 km west of KLRS) showed robust peaks $\sim 1.7 \mu\text{m}$.



280 We believe that (i) the levels of PVSD-shape correspondence found between the AERONET and APS PVSDs as well as the
 281 higher-frequency temporal correspondence between the AERONET CM AOD values and the APS ν_c values and (ii) the purely
 282 optical low-level plume evidence presented above for the July 23, 2007 case (the correspondence between τ_c^P and τ_c^I), lend
 283 credence to a claim of having measured, two independent low-level and optically weak (local) dust events at the Eureka OPAL
 284 site (the CIMEL Δ (CM AOD) increases during both events were respectively $0.007 - 0.004 = 0.003$ and $0.016 - 0.006 = 0.010$).
 285 The detection of such optically weak events (which effectively amount to lower limits of precision in ground-based dust AOD
 286 detectability) help to inform (appreciate certain limitations of) any satellite-based (CM AOD) search for optically detectable
 287 local dust events across the CAA. In the first instance, such weak events would seem to be detectable from a satellite sensor
 288 such as MODIS whose nominal precision appears to be significantly smaller²³. However, MODIS AOD precision is clearly an
 289 excessively optimistic (out of context) statement since that (coarse numeric scale) precision estimate in the presence of very
 290 small AODs would, no doubt, dramatically change (not to mention the fact that the nominal accuracy of the 3 km MODIS
 291 product (± 0.04) is much larger than the nominal precision).



292
 293 **Figure 3 – (a) AERONET inversion PVSDs for the claimed dust event of August 21, 2018, (b) APS hourly-averaged PVSDs at the**
 294 **times of the AERONET PVSDs (with standard deviations shown as error bars). Note that the APS points beyond $\sim 3 \mu\text{m}$ were**
 295 **either superimposed and/or free of counts in a given bin (c) SDA Level 1.5 CM AOD ($\tau_{c,1.5}^0$) and APS ν_c time series and (d) Zoom**

²³ A nominal precision of $0.04 \times \Delta\text{AOD}$ which for our 2018 CM AOD range yields $0.04 \times 0.01 = 0.0004$ (i.e. $0.04 \times \Delta\text{AOD}$ for the best precision case of the 3 km DT over the open-ocean AOD product; Remer et al., 2013).



296 of (c) to the claimed time of the dust event. The triangles shown in (c) indicate the approximate time of the AERONET and APS
297 PVSDs (color coded to match the colors of the 6 PVSD cases in (a) and (b))²⁴.

298 **4.1.3 Satellite imagery versus ground-based measurements at Eureka**

299 The synchronicity between the CM APS v_c and the $\tau_{c,1.5}^0$ time series on August 21, 2018 (after 20:30 UTC) coupled with
300 evidence of what were likely dust plumes over Eureka Sound (notably weak, grey-white plumes that appear to stretch across
301 Eureka Sound²⁵ at and south of the entrance of Slidre Fjord) provide regional evidence for the possibility of a very weak dust
302 event at OPAL (that was probably incited by the strong (generally north to south) winds of Figure S12 as they travelled over
303 the Fosheim Peninsula landmass north of OPAL). While Sentinel-2 clearly sees apparent dust plumes in Eureka sound (that
304 MODIS AOD imagery suggests is $\lesssim 0.03$ ²⁶) even the Sentinel-2 imagery, would likely not detect a sub 0.01 CM AOD (the
305 post 20:30 UTC $\tau_{c,1.5}^0$ OPAL CM AOD values of Figures 3c and 3d): the explicit image evidence for weak plumes over or near
306 the OPAL site is ambiguous at best.

307 Figure 4 shows the temporal variation of the Eureka wind speed (ws) and wind direction for Aug. 21 and 22. The rapid increase
308 at $\sim 21:00$ UTC in the v_c and $\tau_{c,1.5}^0$ time series of Fig. 3c is within the period of significantly high-amplitude ws values from
309 18:00 Aug. 21 to 18:00 Aug. 22 (the red-filled points of Fig. 4). This behavior is broadly consistent with CARA (Copernicus
310 Arctic Regional Reanalysis) near-surface simulations in the neighbourhood of Eureka Sound to the west of OPAL (the region
311 of the Aug. 21 dust plumes in the Sentinel-2 image of Fig. S12). We would argue, based on the CARA spatio-temporal
312 simulations of generally weaker ws values at 18:00 UTC to generally stronger values at 21:00 UTC over the Eureka Sound /
313 OPAL region²⁷, that a significantly strong regional wind event²⁸ incited the Eureka Sound Aug. 21 dust plumes and the attendant
314 v_c and $\tau_{c,1.5}^0$ increases near OPAL (the latter plumes likely being induced by northerly winds traversing the slopes of the
315 Fosheim Peninsula).

316

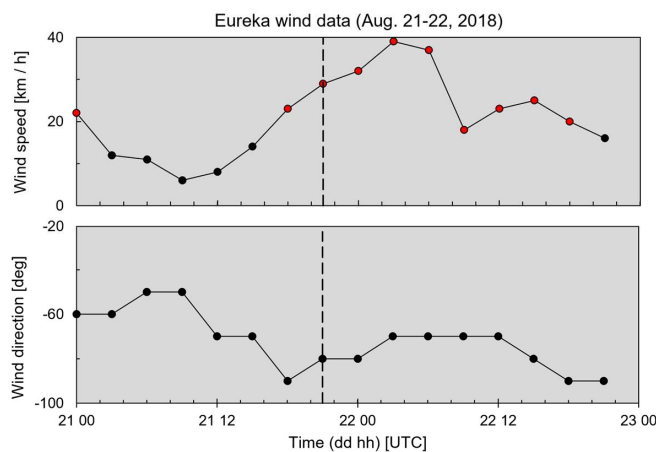
²⁴ Note that the original high-frequency 3D (1 minute sample frequency) time series of APS PSDs are available upon request to the authors.

²⁵ See Figures S12 and S13 in the supplementary PowerPoint file “Satellite_Analysis”. The high spatial resolution (10 m pixels) of the Sentinel-S2A image and the overlaid wind-vector field of Fig. S12 along with the blinking Sentinel-S2A images of 19:49 and 20:40 UTC acquisition times, suggest that dust plumes in Eureka Sound likely originated from the barren western slopes of Axel Heiberg Island.

²⁶ Very spatially coarse AOD pixels of 3 km resolution: Eureka Sound is $\lesssim 3$ MODIS-AOD pixels in width

²⁷ as per Figures S32g and S32h of the Supplementary PowerPoint file “CARA_wind_simulations”

²⁸ Roughly (qualitatively) lasting from 18:00 Aug. 21 (Fig. 32g) to 06:00 Aug. 23 (Fig. 32s).



317

318 **Figure 4 – Temporal variation of the wind speed and wind direction for Aug. 21 and 22, 2018 (data from the ECCC “Eureka Climate”**

319 station very near 0PAL). The wind direction is defined as the direction that the wind is coming from relative to the station meridian.

320 Positive and negative wind directions refer to CW and CCW angular departures from the meridian. The red-filled points indicate

321 wind speeds that are above the mean + standard deviation ($15.5 + 2.5 = 18$ km / h) value of the Eureka (August) windspeed

322 climatology reported in Fig. 5 of Lesins et al. (2010). The dashed vertical line shows a time (21:00 UTC) that is representative of the

323 significant rise in CM AOD ($\tau_{c,1.5}^0$) and APS ν_c values in Fig. 3.

324 **4.2 Satellite-based RS of local dust events across the CAA**

325 We also employed satellite-based RS to investigate potential dust events over CAA sites where there was no ground-based

326 sensors. Our goal here was to gain more general insight into satellite-based RS capabilities in different types of Arctic

327 environments. A strong motivation for the CAA analysis was our belief that satellite-based dust RS findings over a variety of

328 CAA sites would help build confidence in the satellite-based RS of dust events in general and weaker dust events in particular.

329 Each one of our dust event cases below includes a small CAA map with the position of the event indicated by a green star.

330 **4.2.1 Large-scale dust event in the northern part of the CAA**

331 Figure 5a shows an Aqua true color image²⁹ of a dust plume that appears to originate from Axel Heiberg Island³⁰ and flow

332 along the open water of Eureka Sound and Greely Fjord. The thumbnail images of Figures 5b and 5c show respectively, the

²⁹ Acquired at 15:20 UTC (late morning local time) on September 8, 2020

³⁰ it appears to be emanating from the largely barren drainage basin whose watershed empties into Eureka Sound (see Fig. S15).

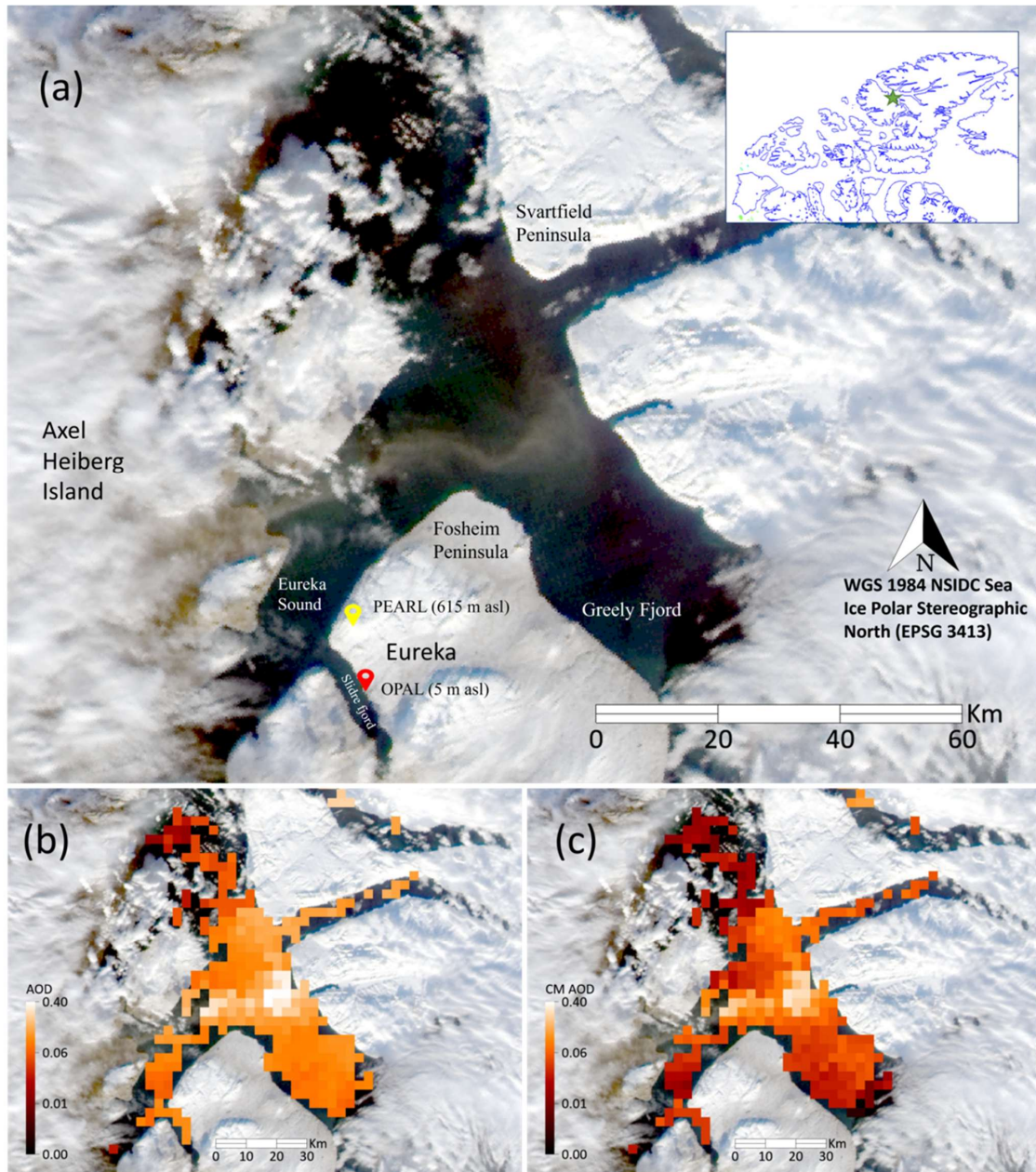


333 MODIS-Aqua AOD and CM AODs (3 km resolution product) superimposed on the color image. Figure S14a³¹ shows a zoom
334 of the Aqua color image blinking with the AOD and CM AOD products alongside a map of the region (we recommend looking
335 at such zooms for details). The plume is most evident as it crosses Greely Fjord along its northeastward path and then appears
336 to veer northwestward towards the coast of the Svartfjeld Peninsula. This flow pattern is generally supported by the surface
337 ws vector field of Fig. S14b (including a final CCW turning (backing) in Greely Fjord followed by a CW turn (veering) of the
338 dust plume towards Svartfjeld Peninsula³²). The CM AOD values of Fig. S14a show a spatial pattern that includes a band of
339 moderately stronger CM AOD values which are coherent with the northeast-flowing spatial pattern of greyish intensity
340 variations in the true-color image (less evident but still notable is the CM AOD and greyish-intensity pattern matching of the
341 weaker plume that has veered in the northwesterly direction). The CM AOD values vary from extremes of ~ 0.02 to 0.31 (AOD
342 extremes of 0.06 to 0.42).

343

³¹ Supplementary PowerPoint file “Satellite_Analysis”

³² There are no MINX (MISR) plume height or speed retrievals to report because the plume was basically obscured by clouds at the MISR orbit time of 19:50 UTC.





345 **Figure 5 – (a) MODIS Aqua true color image acquired at 15:20 UTC on Sept. 8, 2020, (b) and (c) MODIS Aqua AOD product and**
346 **derived CM AOD products respectively (superimposed on the true color image: see Fig. S14a for a detailed (zoomed) overlain**
347 **comparison of (a), (b), and (c)). See Section 3.4.1 above for the expression relating CM AOD to AOD.**

348 **4.2.2 Dust event in the central southern part of the CAA**

349 Figure 6a shows a (Sept. 26, 2015) MODIS-Terra, true color image of local dust plumes apparently emanating from Prince of
350 Wales Island (in the central southern part of the CAA) and moving in a northwesterly direction towards Victoria Island (image
351 acquired at 19:10 UTC). The true color image, along with the MODIS AOD products of Figures 6b and 6c, supported by the
352 MISR stereoscopic multi-look animation (see Fig. S16³³ and its caption for details) reaffirm the presence of dust plumes
353 flowing in a northwesterly direction. The color image and MODIS AOD products of Fig. 6 (see Fig. S17 for greater detail)
354 support a claim of distinct individual dust plumes. The CM AOD and AOD values of the plumes (whose spatial variation is
355 visually coherent with the variations of the plume-like structure seen in the color image) vary respectively, across extremes of
356 0.02 to 0.56 and 0.06 to 0.73). The high-resolution Google Earth landcover map (Fig. S18) shows a 20-km wide barren region
357 which appears to be the dominating influence as the source of the dust plumes (judging by the color image combined with the
358 MODIS AOD product).

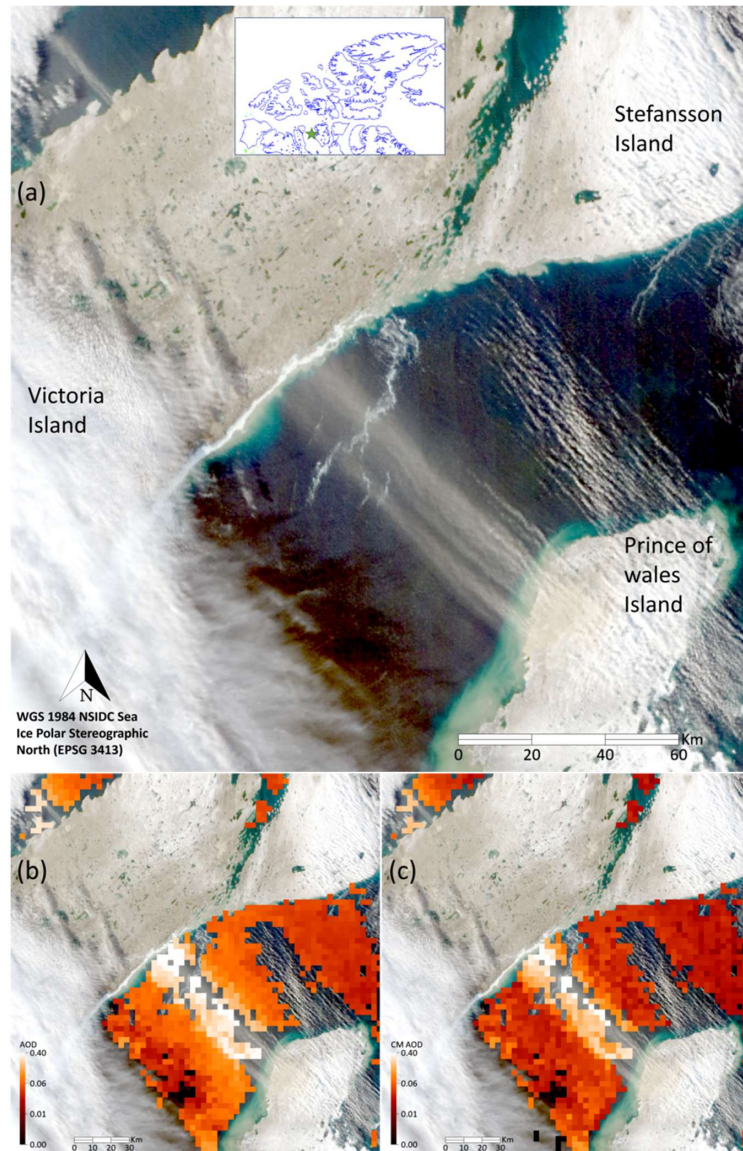
359 A sampled MISR trajectory in the direction of the dust plume (the orange-colored trajectory on the MISR color image of Fig.
360 7a) shows wind-corrected plume height along that trajectory while Figures 7b and 7c show, respectively, plume heights as a
361 function of trajectory-sample number and the plume heights histogram. The analogous pair of trajectory and histogram graphs
362 for plume speed are shown in Figures 7d and 7e. The average MINX (MISR) plume height \pm its standard deviation is $298 \pm$
363 230 m ASL³⁴. The mean and standard deviation of the MISR wind (plume) speed histogram ($\langle ws \rangle \pm \sigma(ws) = 75 \pm 24$ km
364 / h or 54 ± 17 km / h when normalized to near surface conditions³⁵). This $\langle ws \rangle$ value is \sim the 19:00 UTC Sept. 26, 2015
365 Stefansson Island met station ws value of 49 km / h and \sim 3-times the (2002 – 2024) Stefansson Island climatological mean
366 for the month of September (17.7 ± 10.9 km / h).

367

³³ Supplementary PowerPoint file “Satellite_Analysis”

³⁴ We note that in general, neither the plume height or the plume speed sampling trajectories are subject to any objective sampling protocol and that the plume height (and plume speed) histograms generally represent significant departures from a normal distribution. While we report means and standard deviations of plume height and wind speed, they are meant to be order-of-magnitude height and height variability indicators for subjectively selected plume structures seen in the color imagery.

³⁵ An ECCC met station (WMO ID: 71017, coordinates $73^{\circ}46'N, 105^{\circ}18'$) at 11 m elevation is located on Stefansson Island (see Fig. 6). We normalized the MISR plume speed to the plume speed at the elevation of the station by applying a standard wind gradient expression (see .e.g. Kaltschmitt et al., 2007) with an open-water wind shear (Hellman) exponent of 0.1: $ws(h) = ws_{ref}(h/h_{ref})^a$, $ws_{ref} = ws(h)(h/h_{ref})^{-a} = 75(298/11)^{-0.1} = 54$

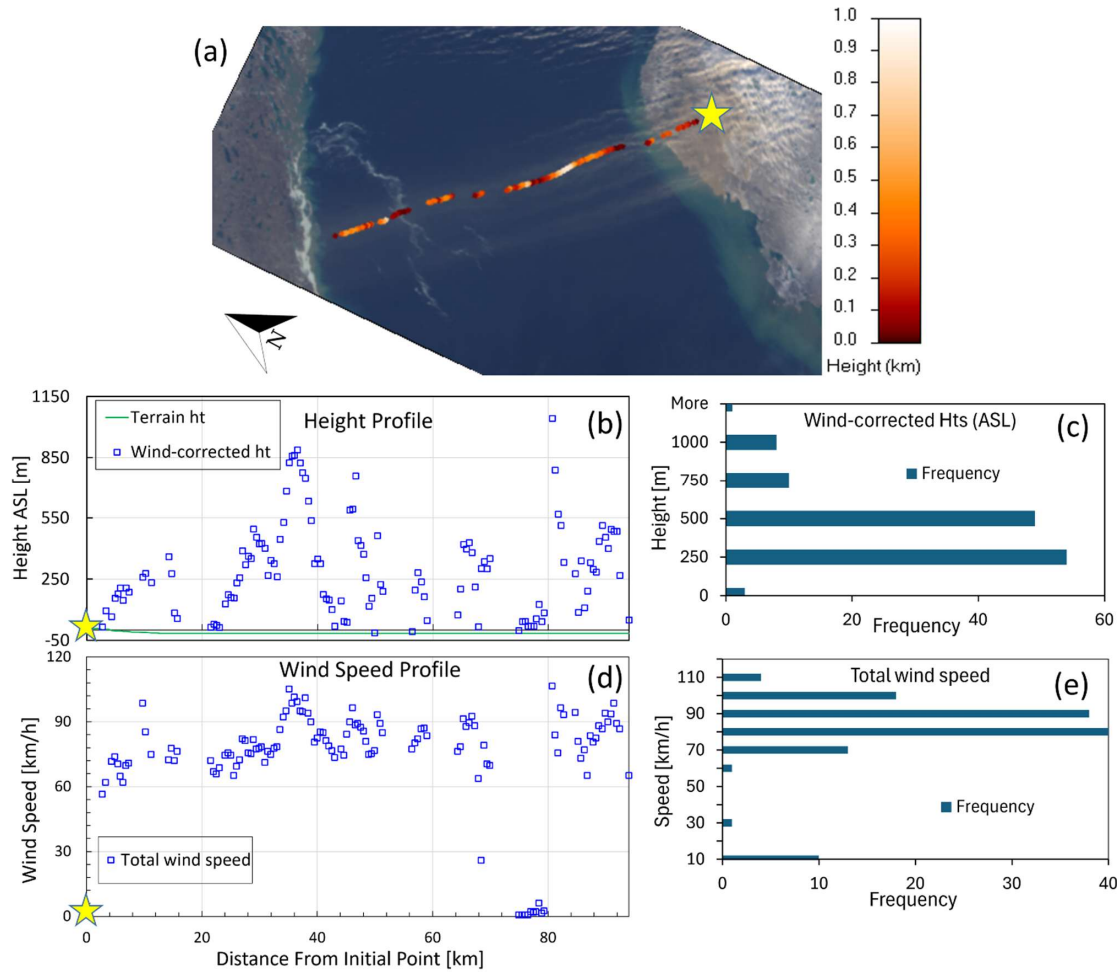


368

369 Figure 6 – local dust event (over Prince of Wales Island and Victoria Island) captured on 26 September 2015. (a) MODIS Terra true-
370 color image acquired at 19:10 UTC (b) AOD product, (c) CM AOD. Note that there appear to be distinct water plumes before and
371 after the barren region on Prince of Wales Island (water plumes that were captured by the MODIS cloud OD product and are
372 distinctly unique in the color image).



373



374

375 **Figure 7 – (a) MISR nadir (An camera) true color image acquired at 19:12 UTC (275 m resolution) with retrieved MISR plume**
376 **height values along a selected trajectory (the red-orange path that begins with a yellow star and whose color legend appears to the**
377 **right of the image) superimposed on the color image, (b) trajectory plume heights as a function of distance from the reference point**
378 **(yellow star) and (c) the histogram of those selected plume heights. The (d) and (e) graphs are the corresponding wind (plume) speed**
379 **trajectory values and histogram. We note that the MINX assumption of no vertical plume motion may reduce the plume height**
380 **retrieval accuracy (Nelson et al., 2013).**

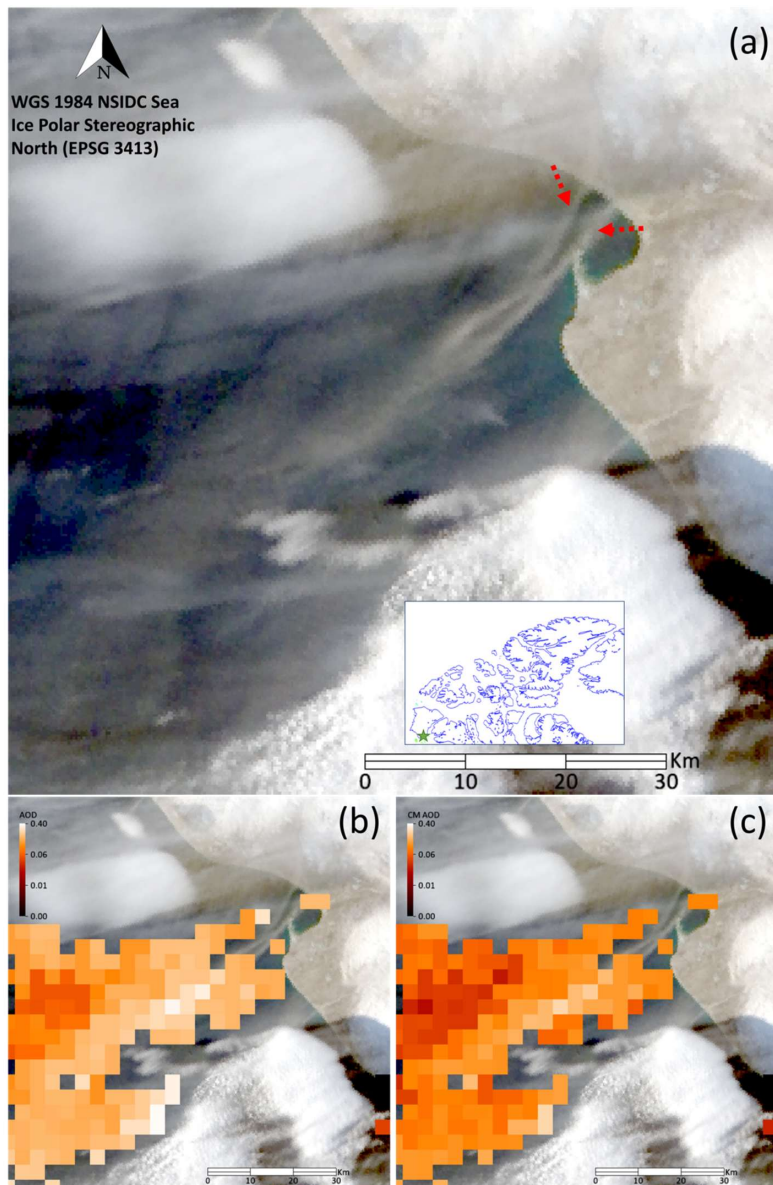


381 **4.2.3 Dust event in the southwest corner of the CAA**

382 The red arrows of Fig. 8a delineate what we argue are a pair of local dust plumes emanating from largely vegetation-free areas
383 on Banks Island (the southwest corner of the CAA) and flowing south over the Amundsen Gulf (MODIS-Terra color image
384 acquired at 20:20 UTC on October 1, 2018). Some plume widths are sufficiently thin that the moderate resolution MODIS and
385 MISR color imagery (as well as the coarser resolution of the MODIS 3 km AOD product) diffuses out much of the fine spatial
386 detail. The AOD product and the derived CM AOD (Figures 8b and 8c) appear to capture the general individual plume patterns
387 seen in the color imagery (and their apparent broadening into a single plume). The MODIS CM AOD values in the vicinity of
388 those plumes range from ~ 0.03 to 0.26 (while AOD values range from ~ 0.04 to 0.37).

389 This was a complicated case with high altitude cirrus being (at least qualitatively) confused with the very low altitude dust
390 plumes. The issue can, on a visual level, be resolved by deferring to animations of the multi-angle MISR views where the
391 separation of the former from the latter (in terms of their apparent stereoscopic ground speed relative to the fixed ground scene)
392 is evident (see that animation in Fig. S19). Figure S20 shows a sampling trajectory of the double dust plumes that are pointed
393 to by the red arrows of Fig. 8a. The mean and standard deviation of the MISR plume height and wind (plume) speed histograms
394 along this trajectory are respectively 196 ± 155 and 25 ± 25 km / h (the latter value belonging to a distinctly non-normal
395 distribution).

396 The geographic details of the two thin dust plumes seen in the MODIS-Terra color image of Fig. 8a along with even weaker
397 and thinner dust plumes elsewhere in the region are brought into rather striking relief in zooms of a high-resolution Sentinel-
398 2 image. Figure S21 shows, what amounts to, apparent source information for five different plumes (including source
399 information for one of the two thin dust plumes seen in the MODIS image). Those zoomed images give valuable, if indirect,
400 contextual information on the source and dynamics of the plumes. One can, for all five cases, see a water to land dust plume
401 continuity with the plume origins being either (a) very low altitude dust plumes over the land or (b) surface features of the
402 sources.



403

404 **Figure 8 – (a)** Local dust plumes emanating from Banks Island on October 1, 2018 (MODIS Terra true color image acquired at
405 20:20 UTC). Figures (b) and (c) show the MODIS Terra AOD and the derived CM AOD superimposed on the color image



406 **4.3.4 Dust plumes emanating from Ellef Ringnes Island (eastern part of the central CAA)**

407 The 20:10 UTC, September 13, 2014 MODIS-Terra true color image of Fig. 9a shows what appear to be local dust plumes
408 emanating from dark brown regions of Meteorologist Peninsula³⁶ and flowing over the open-water region at the southern tip
409 of that peninsula. Figures 9b and 9c show the MODIS AOD product and estimated CM AODs over a part of that open-water
410 region: the spatial variation of those AODs and CM AODs are qualitatively coherent with the perceived spatial variations of
411 the dust plumes in the true color image of Fig. 9a. Figure S23 shows zoomed-in details: one can observe that the thickest part
412 of the plumes as seen on the color image and the largest CM AODs are aligned with the brownish regions (presumably sources)
413 on Meteorologist Peninsula. CM AOD values in Fig. 8b and 8c range from ~ 0.05 to 0.47 while the AOD values range from ~
414 0.11 to 0.50.

415 Figures S24 and S25 show a selected MISR trajectory case over the open water west of Meteorologist Peninsula (Fig. S22
416 shows the [subjective] investigation that was carried out to determine the color image enhancement that best permitted one to
417 appreciate how the trajectory was embedded in the dust plume³⁷). The mean wind-corrected plume height is 264 ± 162 m for
418 the trajectory while the mean plume speed is 38 ± 14 km / h. Normalizing the latter value to the height of the nearest met
419 station³⁸ yields normalized wind speeds of 32 km / h. This is moderately lower than the 20:20 AUT measured value of 51 km
420 / h and 1.7-times its climatologically (1996 – 2025) mean wind speed for the month of September (18.8 ± 13.5 km / h).

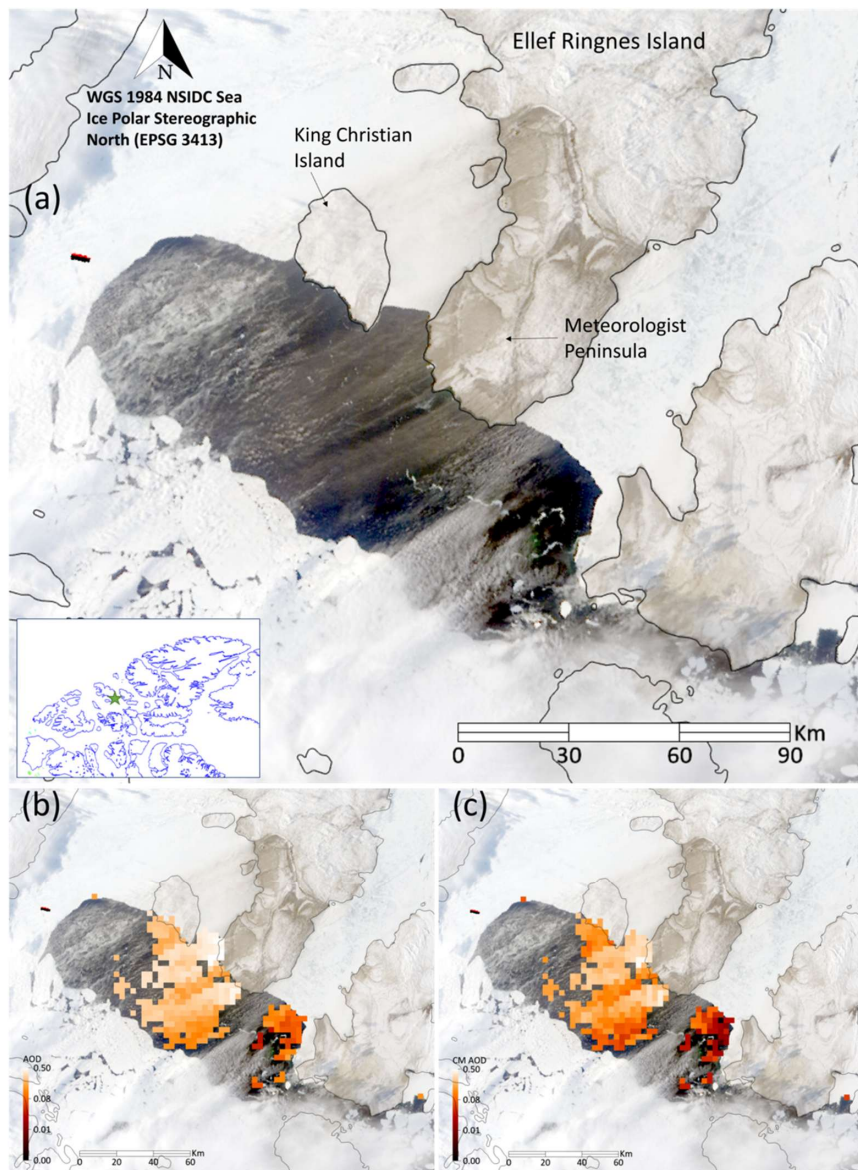
421 In the absence of a standard AOD product we developed an ad hoc AOD retrieval technique for the dirty brown snow/ice
422 region between Meteorologist Peninsula and King Christian Island (see Fig. S26 and its caption for details on that ad hoc
423 technique). The results of that retrieval showed a coarse degree of AOD continuity across the ice/snow to water interface³⁹
424 (see the blinking animation of Fig. S27). Evidence that the dirty brown area was (at least in part) a dust plume and not deposited
425 dust is provided by a MISR height profile showing plume heights varying between 0 to ~ 500 m (Fig. S28). The corresponding
426 plume speeds of 42 ± 20 km / h are moderately greater than the plume speeds over water.

³⁶ Meteorologist Peninsula is located at the extreme south of Ellef Ringnes Island (again, see Fig. 9a)

³⁷ Figure S24 shows the MISR camera animation where one can more readily appreciate the positions and stereoscope movement of higher altitude clouds.

³⁸ The 58 m ECCC met station of “ISACHSEN (AUT)” in the north of Ellef Ringnes Island ($78^{\circ}47'N$, $103^{\circ}33'W$). The normalization approximation for wind-shear (wind gradient) effects was carried out as per Section 4.2.2 above.

³⁹ there is no CM AOD option for the snow/ice retrievals since we have no CMF estimate for those retrievals



427

428 **Figure 9 – MODIS-Terra true color imagery (logarithmic enhancement) acquired at 20:10 UTC over Ellef Ringnes Island on Sept.**
429 **13, 2014 (a) local dust plumes over the water emanating from Meteorologist Peninsula on Ellef Ringnes Island. Figures (b) and (c)**
430 **show the MODIS Terra AOD and derived CM AOD superimposed on the color image (see Fig. S23 in the supplementary**
431 **PowerPoint file “Satellite_Analysis” for a full resolution comparison of the AODs and the color image).**



432 **4.4 Surface plume deposition / snow melt; snow/ice reflectance changes as optical precursors of dust plumes**

433 The RS of airborne Arctic dust can be advantageously complemented by the RS of reflectance changes (darkening) induced
434 by the deposition of airborne dust on snow or ice and/or reduced reflectance incited by premature snow melt due to dust
435 deposition. Woo et al. (1991) noted that the presence of snow-melt zones over the Fosheim Peninsula on Ellesmere Island
436 corresponded to dark spots in early AVHRR imagery. Ranjbar et al. (2021) found roughly the same dark patterns in true color
437 MODIS imagery and showed visual evidence of deposition of dust on snow (or the snow melt product of underlying soil) in a
438 mosaic of true color MODIS imagery acquired over the whole of Ellesmere Island.
439 O'Neill et al. (2025) argued that the combination of persistent day to day dark zones in MODIS imagery and the lack of
440 movement of those features in MISR multi-angle imagery was indicative of local-dust surface deposition in the case of Prince
441 Patrick Island and neighbouring Eglinton Island (west central CAA). We found what appeared to be a more dynamic MISR
442 example of deposited dust across the Strand Bay region of Axel Heiberg Island over a three-day period (see Fig. S29). Figure
443 S30a shows the MISR height profile of a June 8, 2007, airborne dust plume and the position of its sampling trajectory on the
444 associated MISR (nadir) image⁴⁰. The plume profile of Fig. S30b (acquired two days later) shows what appears to be near-
445 zero heights in a region where the color image indicates a much darker pattern than that of Fig. S30a⁴¹ (accompanied by a rise
446 in plume height near the northern shore of Strand Bay). We would suggest that the darkest region of Strand Bay in the color
447 image is likely a dynamic example of the process of dust deposition. In this particular case, the source of the (very dark) dust
448 is likely the volcanic deposits known to characterize much of the Strand Fjord Formation (Williamson & MacRae, 2015).

449 **5 Conclusions**

450 Ground-based RS and microphysical measurements acquired at the PEARL complex in Eureka were employed to investigate
451 the potential for satellite-based and ground-based RS of local dust plumes. This analysis was supported and / or complemented
452 by explicit examples of satellite-based RS of local dust events near Eureka and across the CAA. Ground-based RS validation
453 results were obtained (in terms of the identification and characterization of local dust events) with significant correlations
454 between the OPAL (ground-based) CM AOD and the lidar-derived CM AOD (and the lack of correlation with the 615 m above-
455 plume CM AOD at the Ridge Lab). Comparisons between AERONET and APS PVSDs strongly suggested that both types of
456 instruments were sensitive to local dust PVSD peaks $\sim 1.3 - 1.5 \mu\text{m}$ radius. This was similar to the $1.3 \mu\text{m}$ radius AERONET
457 peaks reported by SDN for a springtime measurement campaign at the KLRS site in the Yukon (a peak which they described
458 as likely being associated with springtime Asian dust). The correlations between APS CM particle-volume concentration
459 (v_c) measurements and OPAL CM AODs along with the similarity between the APS and AERONET PVSDs suggest a
460 significant $1.3 - 1.5 \mu\text{m}$ radius peak that was due to local dust of weak CM AOD ($\lesssim 0.01$).

⁴⁰ The MISR image shows numerous dust plumes which appear to be associated with dark sources on the southern shore of Strand Bay.

⁴¹ Note that the MISR times of S30a and S30b images are nearly identical (solar illumination conditions are nearly identical)



461 Indirect linkages were made between the surface RS and microphysical data and available satellite RS imagery acquired in the
462 neighbourhood of Eureka: we argued that a weak but detectable plume over Eureka Sound (MODIS AODs $\lesssim 0.1$) might be
463 related to the very weak CM AODs measured by the OPAL CIMEL (values of $\lesssim 0.01$ that are typically undetectable by satellite
464 RS). More direct linkages were made with OPAL ws measurements and regional ws (reanalysis) values. It was argued that
465 above normal OPAL ws values and above normal regional ws values coupled with co-incident increases in CM AOD and
466 $v_c(0)$ measurements at OPAL were evidence of a region-wide wind event that caused local and regional dust disturbances.
467 A pan-CAA analysis using the multi-dimensional information available from MODIS color imagery and its AOD products,
468 MISR multi-camera, stereoscopic imagery, MINX (MISR) estimates of plume height and speed and high spatial resolution
469 Sentinel-2 imagery supported by measured and /or regional ws products indicated that local dust plumes of relatively weak to
470 strong optical thickness (CM AOD ranging from ~ 0.02 to 0.60) at generally sub-km plume heights could be detected from
471 available satellite products. A sampling of key parameters for all plume events is given in Table 1. In what follows we give a
472 summary of those pan-CAA conclusions.
473 A plume event north of the Fosheim Peninsula showed evidence of plume dynamics that were roughly coherent with CARRA
474 wind vector patterns and whose spatial variation (pattern) was similar to the spatial pattern of the derived CM AODs. The
475 MINX (MISR) plume height and speed of (September 26, 2015) dust plumes flowing from Prince of Wales Island to Victoria
476 Island (southern part of the CAA) were 300 ± 230 m ASL and 75 ± 24 km / h (while MODIS CM AOD values ranged from
477 0.02 to 0.56). The 54 km / h value⁴² for that event is abnormally large (3 times the climatological mean for September).
478 Information from MISR, MODIS and Sentinel-2 color imagery was employed to identify dust plumes (partially obscured by
479 higher altitude clouds) emanating from local dust sources on Banks Island (southwest corner of the CAA) in October of 2018.
480 The MODIS CM AOD values, for the Banks Island satellite events varied from 0.03 to 0.26 and visually corresponded to
481 what appeared to be dust plumes in the MODIS color imagery (supported by the stereoscopically determined distinctions
482 between clouds and low-level plumes provided by the MISR imagery). The Sentinel-2 color imagery provided a unique high-
483 spatial-resolution perspective that enabled the distinction of the land to water continuity of a few local dust plumes. A
484 moderately strong dust event emanating from Ellef Ringnes Island in September of 2014 was characterized by CM AODs
485 between ~ 0.05 to 0.47, mean plume heights of $\lesssim 300$ m and mean plume speed (normalized to the elevation of the nearby met
486 station) of 32 ± 12 km / h (1.7 times the climatological mean of the nearby [Stefansson Island] met station for the month of
487 September).
488 Finally, we employed MINX (MISR) color imagery and plume height retrievals to argue that June, 2007 Strand Bay (Axel
489 Heiberg Island) MISR images of a dirty snow / ice surface showed both a plume above the surface and what appeared to be
490 plume deposition (zero altitude plume retrievals) over the surface two days later (with a much darker reflectance). This appears
491 to be a rather rare concrete example of a commonly cited phenomenon (dust plume deposition effects).

⁴² the measured value normalized to the height of the nearby met station



492 **Table 1: Summary of CAA dust events captured using satellite-based RS. See footnote 37 concerning the reporting of means and**
 493 **standard deviations for plume height and plume speed.**

Source location (Island)	Date and time (dd/mm/yyyy, hh:mm) [UTC]	Approximate coordinates of plume source (lat, lon) [deg]	AOD (min, max)	CM AOD (min, max)	Visible plume length [km]	plume height (ASL) [m]	plume speed [km/h]
Axel Heiberg Island	08/09/2020, 15:20	(80.05, -87.55)	(0.06, 0.42)	(0.02, 0.31)	60	NA	NA
Prince of Wales Island	26/09/2015, 19:10	(72.65, -102.36)	(0.06, 0.73)	(0.02, 0.56)	110	300 ± 230	75 ± 24
Banks Island	01/10/2018, 20:20	(71.46, -121.74)	(0.04, 0.37)	(0.03, 0.26)	50	196 ± 155	25 ± 25
Ellef Ringnes Island	13/09/2014, 20:10	(77.83, -99.50)	(0.11, 0.50)	(0.05, 0.47)	60	264 ± 162	38 ± 14
Axel Heiberg Island (Strand Bay)	08/06/2007, 19:59	(79, -93.25)	NA	NA	20	165 ± 99	1.6 ± 1.2
Axel Heiberg Island (Strand Bay)	10/06/2007, 19:47	(79, -93.25)	NA	NA	20	40 ± 40	2 ± 2

494

495 **Appendix A**

496 **A1: Comparing CIMEL- and AHSRL-derived AODs**

497 **A1.1: CIMEL-based FM and CM attribution**

498 Given the unique arrangement of the two CIMELS at Eureka, one near the 0PAL site (superscript “O” and one at the higher
 499 altitude PEARL (Ridge lab) site (“P” subscript), the (500 nm) FM, CM and total AODs of the layer between the two sites
 500 (assuming optical homogeneity above P between the two different lines of site) are,

501
$$\Delta\tau_f = \tau_f^0 - \tau_f^P \quad (A1a)$$

502
$$\Delta\tau_c = \tau_c^0 - \tau_c^P \quad (A1b)$$

503 and $\Delta\tau_a = \tau_a^0 - \tau_a^P = \tau_f^0 + \tau_c^0 - (\tau_f^P + \tau_c^P) = \Delta\tau_f + \Delta\tau_c \quad (A1c)$

504 **A1.2: Temporal resampling considerations for the two CIMELs and the lidar**

505 1. $\tau_c^{l,0}$ represents τ_c^l resampled to τ_c^0 times while we use $N^{l,0}$ to describe the number of resampled points.
 506 2. $\tau_c^{P,0}$ represents τ_c^P resampled to τ_c^0 times⁴³ while using $N^{P,0}$ to represent the number of resampled points. $N^{P,0} \neq$
 507 $N^{l,0}$ if, for example, the PEARL measurements are limited in temporal extent relative to the 0PAL temporal extent.

⁴³ but τ_c^P is shown in the PowerPoint profiles



508 3. Accordingly, $\Delta\tau_c$ is more precisely defined as $\tau_c^O - \tau_c^{P,O}$.

509 We employ N^O to represent the common lidar and PEARL resample points ($N^O = N^{l,O} = N^{P,O}$).

510 **A2: FM and CM attributions for the AHSRL lidar**

511 If the FM and CM PDR (particle depolarization ratio⁴⁴) candidates are defined by holistic FM and CM PDR distributions
 512 (whose size-averaged PDRs are δ_f and δ_c) then the optically weighted average VDR can be written as;

513

$$514 \quad VDR = \frac{\delta_f \tau_{\beta,f} + \delta_c \tau_{\beta,c}}{\tau_{\beta,f} + \tau_{\beta,c}} \quad (A2a)^{45}$$

$$515 \quad = \delta_f (1 - \eta_{\beta,c}) + \delta_c \eta_{\beta,c} \quad (A2b)$$

$$516 \quad = \delta_f \eta_{\beta,f} + \delta_c (1 - \eta_{\beta,f}) \quad (A2c)$$

517 where we define

$$518 \quad \eta_{\beta,c} = \frac{\tau_{\beta,c}}{\tau_{\beta,c} + \tau_{\beta,f}} \text{ and } \eta_{\beta,f} = \frac{\tau_{\beta,f}}{\tau_{\beta,c} + \tau_{\beta,f}} = (1 - \eta_{\beta,c}) \quad (A2d)$$

519 As we will argue below, the lidar optical depths (τ_c^l and τ_f^l in the main text⁴⁶) can provide reasonable estimates of τ_c and τ_f
 520 for a strategic choice of δ_{thr} . If the FM and CM PDRs are defined in a binary fashion by a δ_{thr} threshold then those PDRs
 521 can be written,

$$522 \quad \delta_f' = \langle VDR^{\delta \leq \delta_{thr}} \rangle \quad (A3a)$$

$$523 \quad \delta_c' = \langle VDR^{\delta > \delta_{thr}} \rangle \quad (A3b)$$

524 The “ $\langle VDR \rangle$ “ symbolism represents some weighted or unweighted VDR mean in altitude (or in altitude as well as time) where
 525 the δ_{thr} criterion is applied to every single lidar pixel. Equation (A2) represents a tool for seeking out information about the
 526 PDRs of holistic depictions of FM and CM components. One must be wary of the opto-physical differences between δ_f and
 527 δ_c versus δ_f' and δ_c' respectively⁴⁷ and their link with the measured VDR (or averages of measured VDRs). The two
 528 formulations can be investigated by varying δ_{thr} until some optimal solution is obtained for any given event. Part of the process
 529 is the recognition that δ_f is known (empirically and theoretically) to be small (\lesssim a few %; see Fig. A1 for example) while δ_c

⁴⁴ A common label for of a given type of atmospheric particle. See, for example, Liu et al. (2013)

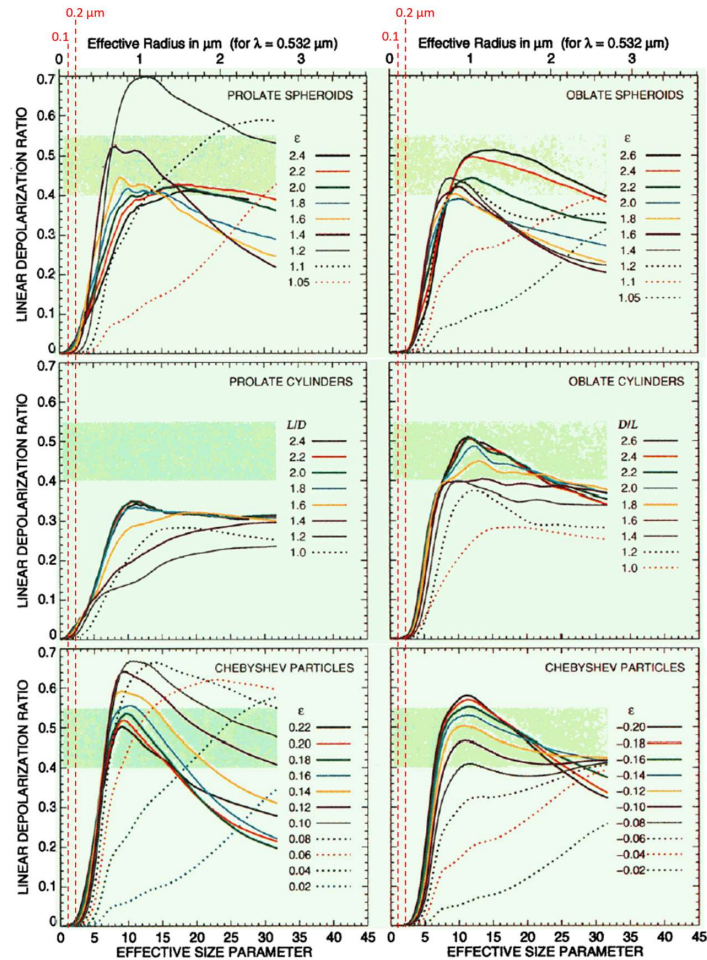
⁴⁵ Where FM and CM (lidar profile) pixels can be defined, respectively by $\delta \leq \delta_{thr}$ & $\delta > \delta_{thr}$ if there is a δ_{thr} saddle between the PDRs

⁴⁶ where $\tau_c^l = S_c \tau_{\beta,c}$ and $\tau_f^l = S_f \tau_{\beta,f}$ (S_c and S_f being their respective lidar ratios)

⁴⁷ Equation (A2) represents a continuously varying function of η_c or η_f while equation A3 is a step function of δ_{thr} (stepping from δ_{thr} -
 dependent values of $\langle VDR \rangle$ for $\delta \leq \delta_{thr}$ to δ_{thr} -dependent values of $\langle VDR \rangle$ for $\delta > \delta_{thr}$)



530 of dust particles generally increases with increasing δ_{thr} in the range where dust-particle population is significant⁴⁸. We
531 suppose that the PDR of other particulate species (clouds, for example) are easily separable from our FM and CM aerosol
532 species.



533
534 **Figure A1 – Computed variation of the 532 nm DR as a function of effective radius (top horizontal scale) and various assumed ice**
535 **particle shapes (Fig. 1 of Mischenko & Sasson, 1998). Optically significant, column-integrated FM particles are largely contained**
536 **within a radius range of 0.1 to 0.2 μm (indicated by the red-dotted vertical lines which we appended to the original figure). This**
537 **demonstrates that the PDR of FM particles is \lesssim a few % for all particle shapes considered by the authors.**

⁴⁸ Where the particle volume sized distribution is significant: see, e.g., Mamouri & Ansmann, 2014 (MA)



538 **A3: The need for vertically-averaged VDR weighting**

539 AHSRL β and VDR profiles (along with derived values of lidar, 0PAL and PEARL CM AODs) for the 7 Eureka dust events
540 that we investigated can be observed in the supplementary PowerPoint file “AHSRL_CIMEL_event_profiles”. The VDR
541 values ranged from small-amplitude negative to positive values to large-amplitude negative and positive outliers (see Section
542 A3.1 for a detailed discussion of how we processed that data). Dörnbrack et al. (2010) reported on airborne lidar observations
543 and characterization of local dust events over Svalbard in May of 2004. Their results included dust plumes whose VDRs ranged
544 from quite small ($\lesssim 5\%$) to values larger than 10% inside the plumes to maximum values of $\lesssim 30\%$ very close to the surface.
545 In the context of the discussion presented in Section A2, VDRs of local dust profiles can achieve (extreme FM to CM) values
546 $\sim 15 - 40\%$ ⁴⁹. MA report that their holistic FM component⁵⁰ produces PDRs ($\sim 5\%$ ⁵¹) while also demonstrating that their sub-
547 μm FM dust tail⁵² can induce a significant VDR increase relative to the holistic FM component⁵³ and that super- μm particles
548 can induce even larger VDRs. See Figures 3a and 3b above for empirical examples showing a super- μm CM peak radius at
549 our 0PAL site (after the advent of the stronger dust event at 20:30 UTC).

550 **A3.1: VDR weighting options.**

551 VDR profile averages ($\langle VDR \rangle$) between 82 and 615 m⁵⁴ were found, in the initial processing run, to be systematically too
552 large⁵⁵. This was suspected to be due to the initial choice of not including negative VDR pixels in any given VDR profile
553 average⁵⁶. Indeed, Fig A2 shows that the simple removal of negative VDR pixels (blue-colored circles) produced $\langle VDR \rangle$

⁴⁹ See, e.g. MA who argue that their FM and CM dust PDRs [“ δ_{df} ” and “ δ_{dc} ” respectively] of 16 and 39% respectively can generate near-source (Sahara) VDR (δ) values of $\sim 31 \pm 3\%$ (the values of Freudenthaler et al., 2009 and Grob et al., 2011 as cited in MA).

⁵⁰ e.g., the complete (and ubiquitous) FM AERONET-inversion component between $\sim 0.05 - 0.2 \mu\text{m}$ (radius) seen in their Fig. 4.

⁵¹ for what they call “non-dust” particles but whose distinctive feature is arguably the limitation to a holistic FM component. See also, for example, the precipitous drop in simulated δ values of ice particles (to magnitudes $< 5\%$) for (ice) between the specific cases of 0.05 and 0.2 μm radius (effective size parameter between 0.6 and 2.4) in Fig. A1.

⁵² the tail of what might be called a holistic CM component between ~ 0.2 to $10 \mu\text{m}$ radius as seen in their Fig. 4

⁵³ MA’s AERONET PSD shows a not insignificant (sub- μm) FM tail of that CM component. It is this tail that surely drives their FM (“ δ_{df} ”) estimate of 16 %.

⁵⁴ the difference in elevation between 0PAL and PEARL (except that the 82.5 m is above the 0PAL elevation of 5 m). The statistics start at 82.5 m because the VDR below 82.5 m was judged to be too noisy.

⁵⁵ too many values well above the typical VDR range for CM dust (see, for example, Fig. 1 of Tian et al., 2020).

⁵⁶ While retaining the rest of the (positive) VDR pixels in the given profile



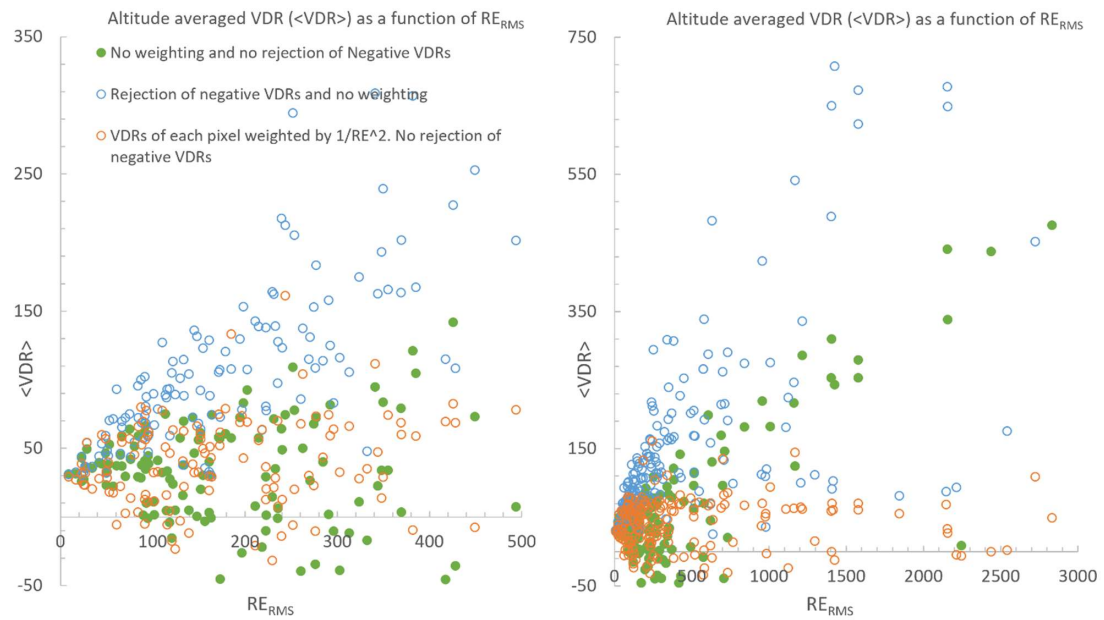
554 estimates that were systematically greater than the two more statistically justifiable methods⁵⁷. Two alternate methods were
555 investigated to mitigate the impacts of removing negative VDRs :

556 ○ The 1st method (green circles) employs no weighting but does not exclude negative VDRs.
557 ○ The 2nd method includes a weighted mean of all VDRs in any given profile ($\langle VDR \rangle_\omega = \sum \omega VDR / \sum \omega$ where $\omega =$
558 $1/RE^2$ for each profile pixel⁵⁸. This takes all VDRs into consideration (does not suffer from the negative-VDR
559 limitations) and seems to produce more realistic $\langle VDR \rangle$ values than the 1st method (values whose $\langle VDR \rangle$ range
560 extends less into (both) the negative region and the positive region. Averaging in time (averaging over the event using
561 an optical weighting factor of τ_β) would then be written as;

562
$$\langle\langle VDR \rangle_\omega \rangle_{\tau_\beta} = \sum \langle VDR \rangle_\omega \tau_\beta / \sum \tau_\beta \quad (A4)$$

⁵⁷ Simply put the exclusion of the negative values acted to increase the $\langle VDR \rangle$ values. This exclusion is debatable given that those negative values could well have a physical sense (they are likely associated with system constants whose range of variability could facilitate the production of negative VDR values for a fraction of the VDRs).

⁵⁸ The “ RE_{RMS} ” of the x axis in Fig. A2 represents the RMS residual error of the individual residual of any lidar pixel in any given vertical profile (the “individual residual” being the difference between a given VDR value at a given altitude and its running average; see the example for two representative lidar profiles in Fig. A3 below). This RE parameter enables an estimation of the noise magnitude by eliminating the systematic trend of the natural VDR variation. . The inverse square weighting approach was inspired by standard texts on linear regression analysis (see, for example, Section 3.5 of Barford, 1967)

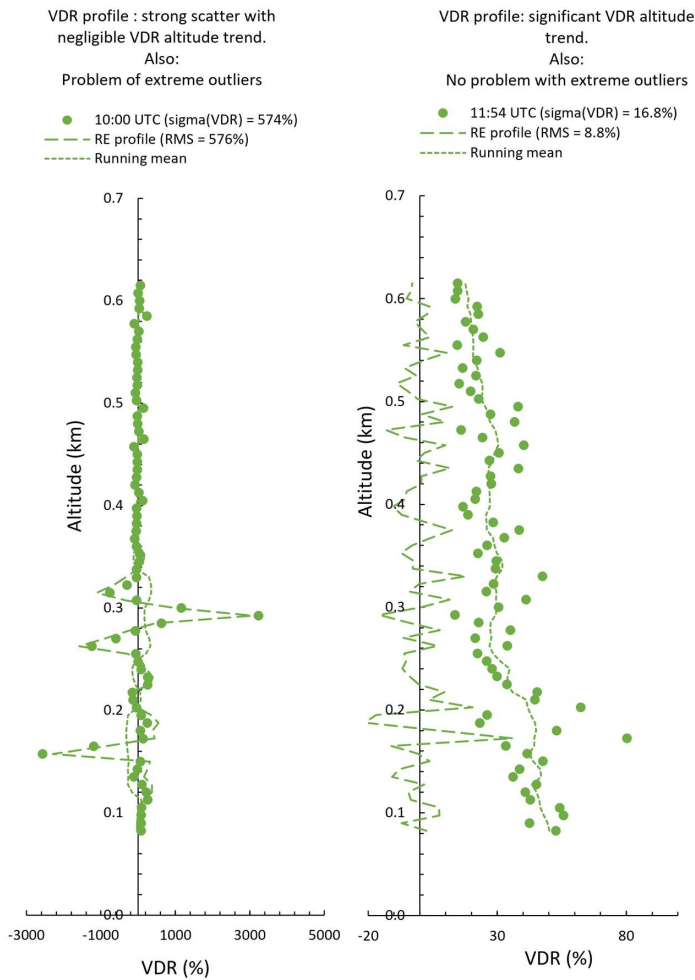


563

564

565 Figure A2 – Altitude-averaged VDRs vs RMS residual errors (RE_{RMS}) for the July 23, 2007 dust event (the LH graph is a zoom of

566 the RH graph). According to our notation, the orange-colored averages should be labelled $\langle VDR \rangle_w$. These statistics were



567

568 **Figure A3 – Two representative lidar profiles (solid-shaded circles), their running mean (dotted curve) and their residual error**
 569 **(RE) difference (dashed curve).**

570 **A3.2: VDR weighting: profile-level impacts and resulting event-averaged statistics.**

571 The impact of the ω weighting discussed in the previous sections is seen in Figures S1b to S7b⁵⁹. In a nutshell the weighting
 572 significantly reduced the intra-profile standard deviations for all events (the bottom graphics of Figures S1b to S7b). We

⁵⁹ Supplementary PowerPoint file “AHSRL_CIMEL_event_profiles”



would also argue that the event-wide average of the intra-profile standard deviation is the best candidate to describe the event-wide precision (noise) of our VDR estimates (see the Fig. S8 caption for details). On the other hand, the weighting introduced a significant amount of VDR variance in 2 events where very little variance existed prior to the weighting process (Events 1 and 6 of Figures S1b and S6b)⁶⁰. The Event 1 and 6 standard deviations of intra-profile, event-level statistics that are summarized in the table of Fig. S8 are accordingly to be treated with caution. Indeed, the table shows explicitly that weighting did dramatically reduce the intra-profile standard deviations of all events excluding Events 1 and 6. We accordingly use the intra-profile statistics in the following section on the derivation of the PDRs for each event.

580 **A3.3: Estimation of the event-averaged CM PDR**

581 Figure A4 shows the event-averaged VDR and τ_β values for both the FM and CM components as a function of δ_{thr} (equation 582 A3 above⁶¹). The CM event averages are rather insensitive to small values of δ_{thr} (arguably because the weak PDR of the 583 FM component and perhaps the weak DR of the sub- μm tail of the holistic CM PDR have little impact at small values of 584 δ_{thr}). They only begin to rise when, we would argue, the sub- μm tail begins to play a more significant optical role (the larger 585 DR of the sub- μm tail incites the beginning of a positive slope that starts to rise at δ_{thr} values ranging from 5 to 15%. A stable 586 estimate of the dust PDR would occur at any value before the rises begin, say at $\delta_{thr} \sim 5\%$

587 That 5% value was chosen to populate the event-dependent 532 nm PDR values of Table A1. Two of the Table A1 values 588 are beyond the (780 nm) VDR upper limit for CM dust found, for example, in Fig. 1 of Tian et 2020 (their upper limit was \sim 589 50% for dust particles ranging in radius from ~ 1 to $5 \mu\text{m}$ ⁶²). On the other hand, all the Table A1 PDR values are largely 590 contained within the 532 nm lidar ratio spread of “giant” near-source Saharan dust particles reported by Esselborn et al. 591 (2009): their Fig. 9 lidar ratios vary between 40 and 60 sr for dust particles of volume median radii ranging from 4 to $15 \mu\text{m}$ 592 (a spread that encompasses the $7 \mu\text{m}$ radius AERONET inversion dust peak that we report above in Fig. 3a). It should be 593 emphasized that choices such as the (“ ω ”) weighting scheme and the optimal δ_{thr} value contain a level of subjective 594 variability (in terms of, for example, the strengths of the weights applied). These factors and other sources of variability 595 produce uncertainties that we estimate as being $\sim \pm$ the “ $\sigma(\text{PDR})$ ” values of Table A1.

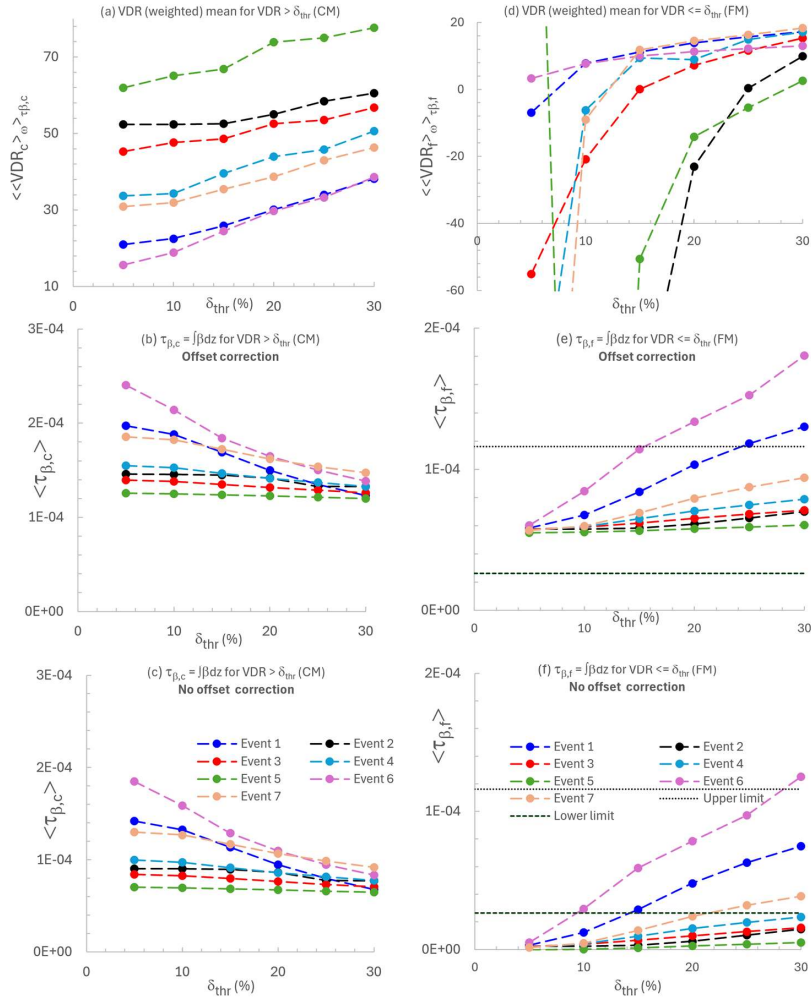
⁶⁰ we could have reduced that variance with an appropriate smoothing approach but decided to forgo that added complication by the simple expedient of choosing the unweighted statistics since those statistics were largely free of the type of extreme VDR variation that one sees in the unweighted VDR means of Events 2, 3, 4, 5 and 7.

⁶¹ to be mathematically precise, those CM event averages (the y axes labels of the LH graphs of Fig. A4) represent $\langle \langle VDR^{\langle \langle VDR \rangle_\omega \rangle_{\tau_\beta} > \delta_{thr}} \rangle_\omega \rangle_{\tau_\beta}$ and $\langle \tau_\beta = \int \beta^{\langle \langle VDR \rangle_\omega \rangle_{\tau_\beta} > \delta_{thr}} dz \rangle$ where the VDR vs δ_{thr} test is applied to each lidar pixel. The RH FM y-axis labels represent $\langle \langle VDR^{\langle \langle VDR \rangle_\omega \rangle_{\tau_\beta} \leq \delta_{thr}} \rangle_\omega \rangle_{\tau_\beta}$ and $\langle \tau_\beta = \int \beta^{\langle \langle VDR \rangle_\omega \rangle_{\tau_\beta} \leq \delta_{thr}} dz \rangle$

⁶² Values which would tend to be moderately larger at 532 nm (see, for example, Table 1 of Mamouri & Ansmann, 2017)



596 The FM VDR averages are significantly more sensitive to δ_{thr} changes at smaller values of that parameter. This is due to a
597 combination of relatively small numbers of VDR pixels being available at small δ_{thr} values and the fact that there seemed to
598 be a small negative bias in the β values. The τ_β weighting across each event then produces wildly oscillating VDR averages
599 at δ_{thr} values of 5 and 10% (Event 2, 3, 4, 5 and 7 cases of Fig. A4d) that were enhanced by the very small τ_β weights in the
600 denominator of the weighting expression. The small negative bias was the cause of unrealistically small $\tau_{\beta,f}$ values for the
601 $\delta_{thr} = 5\%$ case in Fig. A4f. Adding a small β offset to all the β values produced the more realistic “Offset correction” values
602 of Fig. A4f (values that fit into a range of expected $\tau_{\beta,f}$ values between the horizontal dotted lines ; see the caption of Fig.
603 A4 for further details).



604

605 **Figure A4 – VDR averaged results as a function of δ_{thr} for our 7 dust events. LH graphs (CM⁶³ for VDR values $> \delta_{thr}$): (a) Altitude-
 606 and event-averaged VDR_c values (b) $\tau_{\beta,c}$ values with offset correction and (c) $\tau_{\beta,c}$ with no offset correction. RH graphs (d, e, f): the
 607 same array of graphs as the left-hand side but for the FM (VDR values $\leq \delta_{thr}$) . The “offset correction” was a constant offset added
 608 on to β_c and β_f values to eliminate weakly negative β values (due, we presume, to a small calibration inconsistency). The “Lower**

⁶³ the CM component of the “binary” model defined in Section A2 above



609 “limit” and “Upper limit” are roughly-estimated expected bounds⁶⁴ on $\tau_{\beta,f}(0, L)$ (the FM backscatter optical depth across L). These
 610 statistics were computed for the lidar altitude range from 7.5 to 615 m (a more extensive range than that which was reported in the
 611 legend of Fig. A2; tests showed that the averaged VDR values were very similar in the face of such small changes in the profile
 612 range).

Event #	PDR(%)	$\sigma(\text{PDR})$ (%)
1	21	6
2	52	11
3	45	12
4	34	10
5	62	21
6	16	5
7	31	9

613
 614 Table A1 – Dust PDRs for our 7 dust events ($\delta_{thr} = 5\%$). The event colors are consistent with Fig. A4. The precision estimates are
 615 event-averaged, intra profile standard deviations discussed in Section A3.2

616 **A4: Does it help to perform a (ω) weighted CM and FM classification?**

617 If the VDR is so noisy that it requires weighting in the production of altitude-averaged VDRs then the question arises as to
 618 the variability of the VDR-dependent classification of CM and FM aerosols. An approach, which is arguably coherent with
 619 our VDR (residual error) weighting scheme, is to associate the VDR weights (which could be thought of as a “number of
 620 virtual pixels” that increase the importance attributed to a given lidar pixel). Our unweighted FM / CM backscatter AOD
 621 separation is, for the J^{th} lidar-profile at time $t_{i,J}$:

622

$$623 \tau_{\beta c} = \left(\sum_i \beta_{i,J}^{VDR_{i,J} \geq \delta_{thr}} \right) \Delta z \text{ and } \tau_{\beta f} = \left(\sum_i \beta_{i,J}^{VDR_{i,J} < \delta_{thr}} \right) \Delta z \text{ where } \tau_{\beta c} + \tau_{\beta f} = \tau_{\beta} \quad (\text{A5})$$

624

625 This equation explicitly indicates that the $\beta_{i,J}$ summations are mutually exclusive and carried out over all altitude bins of a
 626 given lidar profile. A weighted version of the FM and CM backscatter ODs for lidar profile J⁶⁵, is⁶⁶,

627

$$628 \tau_{\beta c}^{\omega} = K_J \left[\sum_i \omega_{i,J} \beta_{i,J} \right]^{VDR_{i,J} \geq \delta_{thr}} \Delta z \text{ and } \tau_{\beta f}^{\omega} = K_J \left[\sum_i \omega_{i,J} \beta_{i,J} \right]^{VDR_{i,J} < \delta_{thr}} \Delta z \text{ where } \tau_{\beta}^{\omega} = \tau_{\beta c}^{\omega} + \tau_{\beta f}^{\omega} \quad (\text{A6})$$

⁶⁴ The extremes of 0PAL values of τ_f^0 computed for each event using a Eureka (experience-based) estimate of the optically active FM lidar backscatter region (~ 5 to 11 km) and the 0.615 km value of L (the atmospheric layer between 0PAL and PEARL).

⁶⁵ that takes into account the fact that all parameters (those enclosed in the square brackets) must be restricted by the FM and CM conditions

⁶⁶ where $\omega_{i,J}$ is the $1/RE^2$ weighting defined above



629

630 We then force the relation $\tau_{\beta c}^\omega + \tau_{\beta f}^\omega = \tau_\beta$ (this simply means that K_f is set to $\tau_\beta / \tau_\beta^\omega$). Dividing both sides by τ_β yields a
 631 familiar-looking CMF, FMF (CM fraction, FM fraction) type of relation:

632

633 $CMF^\omega + FMF^\omega = 1$ where⁶⁷ (A7a)

634

635 $CMF^\omega = \tau_{\beta c}^\omega / \tau_\beta$ and so $\tau_{\beta c}^\omega = \tau_\beta CMF^\omega$ (A7b)⁶⁸

636

637 $FMF^\omega = \tau_{\beta f}^\omega / \tau_\beta$ and so $\tau_{\beta f}^\omega = FMF^\omega \tau_\beta$ (A7c)

638

639 The $\tau_\beta^\omega = \tau_\beta$ forcing guarantees that the lidar-profile-integrated differences of $\Delta\tau_{\beta f} = \langle \tau_{\beta f} - \tau_{\beta f}^\omega \rangle$ and $\Delta\tau_{\beta c} = \langle \tau_{\beta c} - \tau_{\beta c}^\omega \rangle$
 640 of each profile cancel each other out ($\Delta\tau_{\beta f} + \Delta\tau_{\beta c} = 0$).

641 The results shown in Fig. A5 indicate that the “ ω ” weighting can effectively incite what we attribute to artificial $\Delta\tau_{\beta c}$ and
 642 $\Delta\tau_{\beta f}$ spikes⁶⁹ (the lidar profiles show no corresponding anomalies). These spikes aside, the CM vs FM classification using a
 643 weighting approach generally showed no significant $\tau_{\beta c}^\omega$ vs $\tau_{\beta c}$ changes. Accordingly, any attempt to improve the quality of
 644 $\tau_{\beta c}$ by VDR-noise-based weighting results in either very little change or is the victim of significant outliers generated by the
 645 VDR weighting. Unlike the VDR weighting approach improvements (indicated by Fig. A2) there appears to be no significant
 646 advantage in a VDR-based filtering of the CM / FM classification.

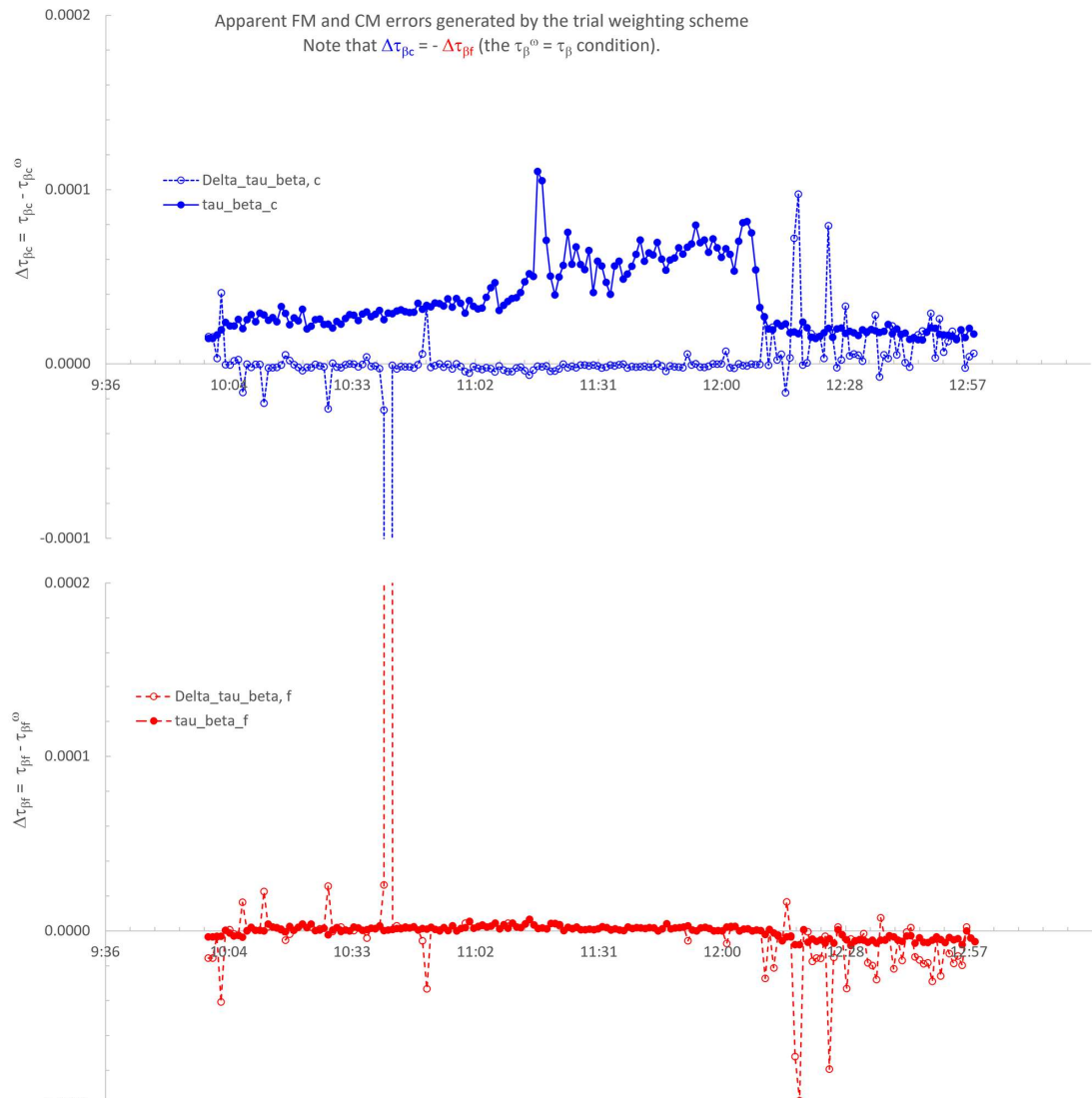
647

⁶⁷ Note that CMF^ω can be > 1 if $\tau_{\beta c}^\omega > \tau_\beta$ (negative β values from the real data and attendant underestimates of τ_β can wreak havoc with the “conservation of unity” equation)

⁶⁸ A heuristic expression (showing explicitly that $0 \leq CMF^\omega \leq 1$) is;

$CMF^\omega = \tau_{\beta c}^\omega / \tau_\beta = [\sum_i \omega_{i,J} \beta_{i,J}]^{VDR_{i,J} \geq \delta_{thr}} \Delta z / [\sum_i \omega_{i,J} \beta_{i,J}] \Delta z = [\sum_i \omega_{i,J} \beta_{i,J}]^{VDR_{i,J} \geq \delta_{thr}} / [\sum_i \omega_{i,J} \beta_{i,J}]$. The explicit link with the unweighted stats is to employ τ_β when calculating $\tau_{\beta c}^\omega$ and $\tau_{\beta f}^\omega$ from CMF^ω .

⁶⁹ The $\omega_{i,J} \beta_{i,J}$ weighting appears to enhance what would otherwise be nondescript points in the $\beta_{i,J}$ profile values.





651 **Appendix B: Acronym and symbol glossary**

652 AERONET : AErosol RObotic NETwork
653 AHSRL: Arctic High Spectral Resolution Lidar
654 AOD: Aerosol Optical Depth
655 APS: Aerodynamic Particle Sizer
656 ASL: Above Sea Level
657 CAA: Canadian Arctic Archipelago
658 CARRA: Copernicus Arctic Regional ReAnalysis
659 CALIOP: Cloud-Aerosol Lidar with Orthogonal Polarization
660 CANDAC: Canadian Network for the Detection of Atmospheric Change
661 CM: Coarse Mode
662 CW: ClockWise
663 CCW : CounterClockWise
664 DB: Deep Blue (MODIS AOD retrieval algorithm over bright surfaces)
665 DT: Dark Target (MODIS AOD retrieval algorithm over dark targets (water and vegetated land)
666 DOD: Dust Optical Depth
667 DR: Depolarisation Ratio
668 FM: Fine Mode
669 HLD: High Latitude Dust
670 MISR: Multi-angle Imaging SpectroRadiometer
671 MODIS: Moderate Resolution Imaging Spectroradiometer
672 NA: Not Available
673 PEARL: Polar Environment Atmospheric Research Laboratory
674 PMSD: Particle-Mass Size Distribution
675 PVSD: Particle-Volume Size Distribution
676 RS: Remote Sensing
677 v_c : Particle-Volume Concentration
678 ws: Wind Speed (km / h)
679 OPAL: Zero Altitude PEARL Auxiliary Laboratory



680 **6 Code availability**

681 MATLAB codes employed for computations reported in this manuscript can be obtained from Seyed Ali Sayedain
682 (seyed.ali.sayedain@usherbrooke.ca).

683 **7 Data availability**

684 AERONET data are available for download at <https://doi.org/10.17616/R3VK9T> (Lind and Gupta, 2023). The PEARL
685 AHSRL data are accessible from the University of Wisconsin HSRL data archives at
686 https://hsrl.ssec.wisc.edu/by_site/2/bscat/2007/07/ (last accessed: 2025-12-02). APS data can be obtained from Seyed Ali
687 Sayedain (seyed.ali.sayedain@usherbrooke.ca). ECCC hourly climate data for different stations can be downloaded at
688 <https://climate-change.canada.ca/climate-data/#/hourly-climate-data> (last accessed: 2025-12-02). MODIS Terra and Aqua
689 images and products along with MISR datasets can be downloaded from the Earth Science Data Systems (ESDS) at
690 <https://search.earthdata.nasa.gov/search>. Sentinel-2 data can be downloaded from Copernicus Browser
691 (<https://browser.dataspace.copernicus.eu/>). CARRA data at different levels (single, pressure, height and model) can be
692 downloaded from the Copernicus Climate Data Store (CDS) at <https://cds.climate.copernicus.eu/datasets>.

693 **8 Supplement**

694 The supplement related to this article is available online at: <https://doi.org/10.5281/zenodo.17794333> (Sayedain and O'Neill,
695 2025).

696 **9 Author contribution**

697 **Seyed Ali Sayedain:** Writing – original draft preparation – review & editing, Visualization, Investigation, Conceptualization,
698 Methodology, Formal analysis, Data curation, Validation, Software, Resources. **Norman T. O'Neill:** Writing – review &
699 editing, Supervision, Visualization, Conceptualization, Methodology, Formal analysis, Data curation, Validation, Funding
700 acquisition, Resources. **Keyvan Ranjbar:** Review & editing, Data curation, Resources. **Phillipe Gauvin-Bourdon:** Review
701 & editing, Data curation, Validation. **Rachel Chang:** Review & editing, Data curation, Validation, Funding acquisition,
702 Resources. **Patrick L. Hayes:** Review & editing, Data curation, Validation, Funding acquisition, Resources. **James King:**
703 Review & editing, Data curation, Validation, Funding acquisition.

704 **10 Competing interests**

705 The authors declare that they have no conflict of interest.



706 **11 Acknowledgements**

707 Valuable in-kind support was provided by the AEROCAN network of Environment and Climate Change Canada (ECCC), the
708 NASA AERONET network, the Canada Research Chairs Program (CRC), and the Canadian Network for the Detection of
709 Atmospheric Change (PAHA/CANDAC) team. We also acknowledge the use of imagery from the NASA Worldview
710 application (<https://worldview.earthdata.nasa.gov>), part of the NASA Earth Science Data and Information System (ESDIS).
711 We also acknowledge the use of Sentinel-2 data from the Copernicus Programme and MISR data provided by NASA. We
712 thank ESA and NASA for making these remote-sensing datasets freely accessible.

713 **12 Financial support**

714 was provided by the Discovery Grant (DG) program of the Natural Sciences and Engineering Research Council of Canada
715 (grant nos. RGPIN-2023-04943, RGPIN-2022-03785, RGPIN-2022-04963), the Canada Research Chairs Program (CRC-
716 2020-00285) and the SACIA-2 (Signatures of Aerosol-Cloud Interaction over the Arctic) project funded by the Canadian
717 Space Agency's ESS-DA (Earth System Science – Data Analysis) program (grant no. 21SUASACOA). SACIA-2 is a
718 collaborative project with Dalhousie University and the Université de Montréal.

719 **References**

720 AboEl-Fetouh, Y., O'Neill, N. T., Ranjbar, K., Hesaraki, S., Abboud, I., & Sobolewski, P. S.: Climatological-Scale
721 Analysis of Intensive and Semi-intensive Aerosol Parameters Derived From AERONET Retrievals Over the Arctic. *Journal*
722 *of Geophysical Research: Atmospheres*, 125(10). <https://doi.org/10.1029/2019jd031569>, 2020.

723 Arnalds, O.: Dust sources and deposition of aeolian materials in Iceland. *Icelandic Agricultural Sciences*, 23, 3–21.
724 https://www.moldin.net/uploads/3/9/3/3/39332633/olafur_arnalds_2010_jas.pdf (accessed: 2025-11-22), 2010.

725 Adams, P., & Dunbar, M.: Arctic Archipelago. In *The Canadian Encyclopedia*. Available at:
726 <https://www.thecanadianencyclopedia.ca/en/article/arctic-archipelago> (last accessed: 2025-11-22), 2015.

727 Bachelard, J., Cadieux, M., Liu-Kang, C., Lambert, P., Filoche, A., Galhardi, J. A., Hadioui, M., Chaput, A., Bastien-
728 Thibault, M. P., Wilkinson, K. J., King, J., & Hayes, P. L.: Chemical and microphysical properties of wind-blown dust near
729 an actively retreating glacier in Yukon, Canada. *Aerosol Science and Technology*, 54(1), 2–20.
730 <https://doi.org/10.1080/02786826.2019.1676394>, 2020.

731 Baddock, M., Hall, A., Rideout, J., Bryant, R., Bullard, J., & Gassó, S.: Satellite observations of Arctic blowing dust events
732 >82°N. *Weather*, 1–6. <https://doi.org/10.1002/wea.7617>, 2024.

733 Barford, N. C., Experimental measurements: precision, error and truth, Addison-Wesley Publishing Company, Inc., Don
734 Mills, Ontario, ISBN 10: 0201003953, ISBN 13: 9780201003956, 1967.



735 Barr, S. L., Wyld, B., McQuaid, J. B., Neely Iii, R. R., & Murray, B. J.: Southern Alaska as a source of atmospheric mineral
736 dust and ice-nucleating particles, *Sci. Adv.*, 9, eadg3708. <https://doi.org/10.1126/sciadv.adg3708>, 2023.

737 Bullard, J. E., Matthew, B., Tom, B., John, C., Eleanor, D., Diego, G., Santiago, G., Gudrun, G., Richard, H., Robert, M.,
738 Cheryl, M.-N., Tom, M., Helena, S., & Thorsteinsson, T.: High latitude dust in the Earth system, *Rev. Geophys.*, 54, 447 485.
739 <https://doi.org/10.1002/2016RG000518>, 2016.

740 Eloranta, E. W., I. A. Razenkov, J. P. Garcia, & J. Hedrick, -, 22nd International Laser Radar Conference, July 12-16,
741 Matera, Italy, 2004.

742 Dörnbrack, A., Stachlewska, I. S., Ritter, C., & Neuber, R.: Aerosol distribution around Svalbard during intense easterly
743 winds. *Atmospheric Chemistry and Physics*, 10(4), 1473–1490. <https://doi.org/10.5194/ACP-10-1473-2010>, 2010.

744 Dubovik, O., Holben, B., Eck, T. F., Smirnov, A., Kaufman, Y. J., King, M. D., Tanré, D., & Slutsker I.: Variability of
745 absorption and optical properties of key aerosol types observed in worldwide locations. *Journal of the atmospheric sciences*.
746 59(3):590–608. [https://doi.org/10.1175/1520-0469\(2002\)059<0590:VOAAOP>2.0.CO;2](https://doi.org/10.1175/1520-0469(2002)059<0590:VOAAOP>2.0.CO;2), 2002.

747 Esselborn, M., Wirth, M., Fix, A., Weinzierl, B., Rasp, K., Tesche, M., & Petzold, A.: Spatial distribution and optical
748 properties of Saharan dust observed by airborne high spectral resolution lidar during SAMUM 2006. *Tellus B Chem. Phys.*
749 *Meteorol.* 61, 131–143. <https://doi.org/10.1111/j.1600-0889.2008.00394.x>, 2009.

750 Garay, M. J., Witek, M. L., Kahn, R. A., Seidel, F. C., Limbacher, J. A., Bull, M. A., Diner, D. J., Hansen, E. G.,
751 Kalashnikova, O. V., Lee, H., Nastan, A. M., & Yu, Y.: Introducing the 4.4 km spatial resolution Multi-Angle Imaging
752 SpectroRadiometer (MISR) aerosol product, *Atmos. Meas. Tech.*, 13, 593–628. <https://doi.org/10.5194/amt-13-593-2020>,
753 2020.

754 Giles, D. M., Sinyuk, A., Sorokin, M. G., Schafer, J. S., Smirnov, A., Slutsker, I., Eck, T. F., Holben, B. N., Lewis, J. R.,
755 Campbell, J. R., Welton, E. J., Korkin, S. V., & Lyapustin, A. I.: Advancements in the Aerosol Robotic Network (AERONET)
756 Version 3 database – automated near-real-time quality control algorithm with improved cloud screening for Sun photometer
757 aerosol optical depth (AOD) measurements, *Atmos. Meas. Tech.*, 12, 169–209. <https://doi.org/10.5194/amt-12-169-2019>,
758 2019.

759 Groot Zwaftink, C. D., Grythe, H., Skov, H., & Stohl, A.: Substantial contribution of northern high-latitude sources to
760 mineral dust in the Arctic, *J. Geophys. Res.*, 121, 13678–13697. <https://doi.org/10.1002/2016JD025482>, 2016.

761 Hansen J. E. and Travis L. D.: Light scattering in planetary atmospheres, *Space science reviews*. 16(4):527-610.
762 <https://doi.org/10.1007/BF00168069>, 1974.

763 Huang, Y., Adebiyi, A. A., Formenti, P., & Kok, J. F.: Linking the different diameter types of aspherical desert dust
764 indicates that models underestimate coarse dust emission. *Geophysical Research Letters*, 48, e2020GL092054.
765 <https://doi.org/10.1029/2020GL092054>, 2021.



766 Justice, C. O., Townshend, J. R. G., Vermote, E. F., Masuoka, E., Wolfe, R. E., Saleous, N., Roy, D. P., & Morisette, J. T.:
767 An overview of MODIS Land data processing and product status. *Remote Sensing of Environment*, 83(1–2), 3–15.
768 [https://doi.org/10.1016/S0034-4257\(02\)00084-6](https://doi.org/10.1016/S0034-4257(02)00084-6), 2002.

769 Kahn, R. A., Li, W.-H., Moroney, C., Diner, D. J., Martonchik, J. V., & Fishbein, E.: Aerosol source plume physical
770 characteristics from space-based multiangle imaging, *Journal of Geophysical Research Atmospheres*, 112, D11205.
771 <https://doi.org/10.1029/2006JD007647>, 2007.

772 Kaltschmitt, M., Streicher, W., & Wiese, A.: *Renewable Energy – Technology, Economics and Environment (XXXII)*.
773 Berlin, Heidelberg, New York, Springer. ISBN 3-540-70947-9, ISBN 978-3-540-70947-3, Page 55. Available at:
774 <http://www.springer.com/us/book/9783540709473> (last accessed: 2025-11-22), 2007.

775 Kawai, K., Matsui, H., & Tobe, Y.: Dominant Role of Arctic Dust With High Ice Nucleating Ability in the Arctic Lower
776 Troposphere. *Geophysical Research Letters*, 50(8), 1–10. <https://doi.org/10.1029/2022GL102470>, 2023.

777 Lesins, G., Duck, T. J., & Drummond, J. R.: Climate trends at Eureka in the Canadian high arctic. *Atmosphere-Ocean*, 48(2), 59–80. <https://doi.org/10.3137/AO1103.2010>, 2010.

778 Levy, R., Hsu, C., et al., : MODIS Atmosphere L2 Aerosol Product. NASA MODIS Adaptive Processing System, Goddard
779 Space Flight Center, USA: http://dx.doi.org/10.5067/MODIS/MOD04_3K_061, 2015a.

780 Levy, R., Hsu, C., et al.,: MODIS Atmosphere L2 Aerosol Product. NASA MODIS Adaptive Processing System, Goddard
781 Space Flight Center, USA: http://dx.doi.org/10.5067/MODIS/MYD04_3K_061, 2015b.

782 Levy, R., Hsu, C., et al., : MODIS Atmosphere L2 Aerosol Product. NASA MODIS Adaptive Processing System, Goddard
783 Space Flight Center, USA: http://dx.doi.org/10.5067/MODIS/MOD04_L2_061, 2015c.

784 Levy, R., Hsu, C., et al.,; MODIS Atmosphere L2 Aerosol Product. NASA MODIS Adaptive Processing System, Goddard
785 Space Flight Center, USA: http://dx.doi.org/10.5067/MODIS/MYD04_L2_061, 2015d.

786 Lind, E. and Gupta, P.: AERONET, Registry of Research Data Repositories [data set], <https://doi.org/10.17616/R3VK9T>
787 (last accessed: 2025-12-02), 2023.

788 Liu, Z., Fairlie, T. D., Uno, I., Huang, J., Wu, D., Omar, A., Kar, J., Vaughan, M., Rogers, R., Winker, D., Trepte, C., Hu,
789 Y., Sun, W., Lin, B., & Cheng, A.: Transpacific transport and evolution of the optical properties of Asian dust, *Journal of
790 Quantitative Spectroscopy & Radiative Transfer*, 116, 24–33. <https://doi.org/10.1016/j.jqsrt.2012.11.011>, 2013.

791 Mamouri, R. E. & Ansmann, A.: Fine and coarse dust separation with polarization lidar, *Atmos. Meas. Tech.*, 7, 3717–
792 3735. <https://doi.org/10.5194/amt-7-3717-2014>, 2014.

793 Mamouri, R. E. & Ansmann, A.: Potential of polarization/Raman lidar to separate fine dust, coarse dust, maritime, and
794 anthropogenic aerosol profiles, *Atmos. Meas. Tech.*, 10, 3403–3427. <https://doi.org/10.5194/amt-10-3403-2017>, 2017.

795 Martonchik, J. V., Diner, D. J., Kahn, R. A., Ackerman, T. P., Verstraete, M. M., Pinty, B., & Gordon, H. R.: Techniques
796 for the retrieval of aerosol properties over land and ocean using multiangle imaging. *IEEE Transactions on Geoscience and
797 Remote Sensing*, 36(4), 1212–1227. <https://doi.org/10.1109/36.701027>, 1998.



799 Meinander, O., Dagsson-Waldhauserova, P., Amosov, P., Aseyeva, E., Atkins, C., Baklanov, A., Baldo, C., Barr, S. L.,
800 Barzycka, B., Benning, L. G., Cvetkovic, B., Enchilik, P., Frolov, D., Gassó, S., Kandler, K., Kasimov, N., Kavan, J., King,
801 J., Koroleva, T., Krupskaya, V., Kulmala, M., Kusiak, M., Lappalainen, H. K., Laska, M., Lasne, J., Lewandowski, M., Luks,
802 B., McQuaid, J. B., Moroni, B., Murray, B., Möhler, O., Nawrot, A., Nickovic, S., O'Neill, N. T., Pejanovic, G., Popovicheva,
803 O., Ranjbar, K., Romanias, M., Samonova, O., Sanchez-Marroquin, A., Schepanski, K., Semenkov, I., Sharapova, A.,
804 Shevnina, E., Shi, Z., Sofiev, M., Thevenet, F., Thorsteinsson, T., Timofeev, M., Umo, N. S., Uppstu, A., Urupina, D., Varga,
805 G., Werner, T., Arnalds, O., & Vukovic Vimic, A.: Newly identified climatically and environmentally significant high-latitude
806 dust sources. *Atmospheric Chemistry and Physics*, 22(17), 11889–11930. <https://doi.org/10.5194/acp-22-11889-2022>, 2022.

807 Met Office, Beaufort, National Meteorological Library and Archive, Fact sheet 6 – The Beaufort Scale. Available at:
808 https://www.metoffice.gov.uk/binaries/content/assets/metofficegovuk/pdf/research/library-and-archive/library/publications/factsheets/factsheet_6-the-beaufort-scale_2023.pdf (last accessed: 2025-11-22), 2010.

809 Mishchenko, M. I., & Sassen, K.: Depolarization of lidar returns by small ice crystals: An application to contrails,
810 Geophysical Research Letters, 25(3), 309–312. <https://doi.org/10.1029/97GL03764>, 1998.

811 MISR Handbook: Multi-angle Imaging SpectroRadiometer Project Handbook, *Atmospheric Science Data Center*, NASA
812 Langley Research Center. Available at: https://asdc.larc.nasa.gov/documents/misr/guide/misr_ov2.pdf (last accessed: 2024-
813 12-21), 2000.

814 Nelson, D. L., Garay, M. J., Kahn, R. A., & Dunst, B. A.: Stereoscopic height and wind retrievals for aerosol plumes with
815 the MISR INteractive eXplorer (MINX). *Remote Sensing*, 5(9), 4593–4628. <https://doi.org/10.3390/rs5094593>, 2013.

816 O'Neill, N. T., Ranjbar, K., Ivănescu, L., Blanchard, Y., Sayedain, S. A., & AboEl-Fetouh, Y.: Remote-sensing
817 detectability of airborne Arctic dust, *Atmos. Chem. Phys.*, 25, 27–44, <https://doi.org/10.5194/acp-25-27-2025>, 2025.

818 Ranjbar, K., O'Neill, N. T., Ivănescu, L., King, J., & Hayes, P. L.: Remote sensing of a high-Arctic, local dust event over
819 Lake Hazen (Ellesmere Island, Nunavut, Canada). *Atmospheric Environment*, 246, 118102.
820 <https://doi.org/10.1016/j.atmosenv.2020.118102>, 2021.

821 Remer, L. A., Mattoo, S., Levy, R. C., & Munchak, L. A.: MODIS 3 km aerosol product: algorithm and global perspective,
822 Atmos. Meas. Tech., 6, 1829–1844. <https://doi.org/10.5194/amt-6-1829-2013>, 2013.

823 Sayedain, S. A., O'Neill, N. T., King, J., Hayes, P. L., Bellamy, D., Washington, R., Engelstaedter, S., Vicente-Luis, A.,
824 Bachelder, J., & Bernhard, M.: Detection and analysis of Lhù'aàn Man' (Kluane Lake) dust plumes using passive and active
825 ground-based remote sensing supported by physical surface measurements. *Atmospheric Measurement Techniques*, 16(17),
826 4115–4135. <https://doi.org/10.5194/amt-16-4115-2023>, 2023.

827 Sayedain, S. A., & O'Neill, N. T.: Remote sensing of local-dust across the Canadian Arctic - Supplementary Material. In
828 Atmospheric Measurement Techniques. Zenodo. <https://doi.org/10.5281/zenodo.1779433>, 2025.



830 Sayer, A. M., Munchak, L. A., Hsu, N. C., Levy, R. C., Bettenhausen, C., & Jeong, M.-J.: MODIS Collection 6 aerosol
831 products: Comparison between Aqua's e-Deep Blue, Dark Target, and "merged" data sets, and usage recommendations,
832 *Journal of Geophysical Research: Atmospheres*, 119, 13,965–13,989. <https://doi.org/10.1002/2014JD022453>, 2014.

833 Sayer, A., Personal communication, 2025.

834 Sinyuk, A., Holben, B. N., Eck, T. F., Giles, D. M., Slutsker, I., Korkin, S., Schafer, J. S., Smirnov, A., Sorokin, M., &
835 Lyapustin, A.: The AERONET Version 3 aerosol retrieval algorithm, associated uncertainties and comparisons to Version 2.
836 *Atmospheric Measurement Techniques*. Jun 26;13(6):3375-411. <https://doi.org/10.5194/amt-13-3375-2020>, 2020.

837 Song, Q., Zhang, Z., Yu, H., Ginoux, P., & Shen, J.: Global dust optical depth climatology derived from CALIOP and
838 MODIS aerosol retrievals on decadal timescales: regional and interannual variability, *Atmos. Chem. Phys.*, 21, 13369–13395.
839 <https://doi.org/10.5194/acp-21-13369-2021>, 2021.

840 Tian, Y., Pan, X., Wang, Z., Wang, D., Ge, B., Liu, X., Zhang, Y., Liu, H., Lei, S., Yang, T., Fu, P., Sun, Y., & Wang, Z.:
841 Transport patterns, size distributions, and depolarization characteristics of dust particles in East Asia in spring 2018, *Journal*
842 of *Geophysical Research: Atmospheres*, 125(16):e2019JD031752. <https://doi.org/10.1029/2019JD031752>, 2020.

843 Tobe, Y., Adachi, K., DeMott, P. J., Hill, T. C. J., Hamilton, D. S., Mahowald, N. M., Nagatsuka, N., Ohata, S., Uetake,
844 J., Kondo, Y., & Koike, M.: Glacially sourced dust as a potentially significant source of ice nucleating particles. *Nature*
845 *Geoscience*, 12(4), 253–258. <https://doi.org/10.1038/s41561-019-0314-x>, 2019.

846 TSI Incorporated, *Aerodynamic Particle Sizer® (APSTM) Model 3321* [Specification sheet]. Available at:
847 <https://www.tsi.com/getmedia/7fd20aa0-8540-4b8d-8572-d164366dd08c/3321-Spec-Sheet-US?ext=.pdf> (last accessed:
848 2025-01-11), 2022.

849 Uno, I., Eguchi, K., Yumimoto, K., Takemura, T., Shimizu, A., Uematsu, M., Liu, Z., Wang, Z., Hara, Y., & Sugimoto,
850 N.: Asian dust transported one full circuit around the globe. *Nature Geoscience*, 2(8), 557–560.
851 <https://doi.org/10.1038/ngeo583>, 2009.

852 Weitkamp, C.: Lidar: range-resolved optical remote sensing of the atmosphere, Springer Science & Business Media, New
853 York (HSRL chapter 5 by E. Eloranta), 2005.

854 Williamson, M. -C. & MacRae, R. A.: Mineralization potential in volcanic rocks of the Strand Fiord Formation and
855 associated intrusions, Axel Heiberg Island, Nunavut, Canada. Geological Survey of Canada, Open File, 7981, 34. Natural
856 Resources Canada. <https://doi.org/10.4095/297365>, 2015.

857 Witek, M. L., Garay, M. J., Diner, D. J., Bull, M. A., Seidel, F. C., Nastan, A. M., & Hansen, E. G.: Introducing the MISR
858 level 2 near real-time aerosol product. *Atmospheric Measurement Techniques*, 14(8), 5577–5591. <https://doi.org/10.5194/amt-14-5577-2021>, 2021.

860 Woo, M. K., Edlund, S. A., & Young, K. L.: Occurrence of early snow-free zones on Fosheim Peninsula, Ellesmere Island,
861 Northwest Territories. *Current Research, Part B, Geological Survey of Canada Paper*, 91, 9-14, ISBN: 0-660-56282-0.



862 Available at: https://publications.gc.ca/collections/collection_2017/rnccan-nrcan/M44-91-1B.pdf (last accessed: 2025-11-22),
863 1991.

864 Xi, Y., Xu, C., Downey, A., Stevens, R., Bachelard, J. O., King, J., Hayes, P. L., & Bertram, A. K.: Ice nucleating properties
865 of airborne dust from an actively retreating glacier in Yukon, Canada. *Environmental Science: Atmospheres*, 2(4), 714–726.
866 <https://doi.org/10.1039/d1ea00101a>, 2022.

867 Yang, S., Preißler, J., Wiegner, M., von Löwis, S., Petersen, G. N., Parks, M. M., & Finger, D. C.: Monitoring dust events
868 using doppler lidar and ceilometer in Iceland. *Atmosphere*, 11(12), 1–23. <https://doi.org/10.3390/atmos11121294>, 2020.

869 Zhao, X., Huang, K., Fu, J. S., & Abdullaev, S. F.: Long-range transport of Asian dust to the Arctic: identification of
870 transport pathways, evolution of aerosol optical properties, and impact assessment on surface albedo changes. *Atmospheric
871 Chemistry and Physics*, 22(15), 10389–10407. <https://doi.org/10.5194/acp-22-10389-2022>, 2022.